Research Square

Preprints are preliminary reports that have not undergone peer review.
They should not be considered conclusive, used to inform clinical practice,
or referenced by the media as validated information.

A multi-region nonlinear model for fatigue life prediction of 3D woven composites under combined tension and bending fatigue

Shuang Qiu

qiushuang@nuaa.edu.cn

Nanjing University of Aeronautics and Astronautics

Haitao Cui

Nanjing University of Aeronautics and Astronautics

Hongjian Zhang

Nanjing University of Aeronautics and Astronautics

Lei Zhou

Nanjing University of Aeronautics and Astronautics

Research Article

Keywords: Woven composite, CCF, Nonlinear model, Life prediction, Damage accumulation

Posted Date: November 5th, 2026

DOI: https://doi.org/10.21203/rs.3.rs-11186517/v1

License: This work is licensed under a Creative Commons Attribution 4.0 International License.
Read Full License

Additional Declarations: No competing interests reported.

A multi-region nonlinear model for fatigue life prediction of 3D woven composites under combined tension and bending fatigue

Shuang Qiu[a,*]; Haitao Cui[a,b,c] ; Hongjian Zhang[a,b]; Lei Zhou[a]

[a] College of Energy & Power Engineering, Nanjing University of Aeronautics and Astronautics, Jiangsu 210016, PR China

[b] Aero-engine Thermal Environment and Structure Key Laboratory of Ministry of Industry and Information Technology, Nanjing University of Aeronautics and Astronautics, Jiangsu 210016, PR China

[c] State Key Laboratory of Mechanics and Control of Mechanical Structures, Nanjing University of Aeronautics and Astronautics, Jiangsu 210016, PR China

ABSTRACT

This paper develops a multi-region nonlinear model to characterize fatigue performance and predict fatigue life of three dimensional woven composites (3DWCs) under combined high and low cycle fatigue (CCF). The model introduces the HCF and LCF stress ratio threshold and fatigue damage threshold to classify fatigue damage into enhanced, fuzzy, and weakened regions. Then, it introduces fatigue life prediction approaches for different fatigue regimes. Also, a novel biaxial experimental platform, including the longitudinal tensile system, the lateral excitation system, and the dynamic signal monitoring system, is established. Based on this platform, some available test data are applied to validate the proposed model. Results indicate that the approach can obtain higher prediction accuracy than others.

Key words: Woven composite; CCF; Nonlinear model; Life prediction; Damage accumulation

1. Introduction

The lightweight design of aero-engine fan blades, an aerodynamic component in the cold section, is an effective approach for improving engine performance and fuel efficiency [1]. Three-dimensional woven composites (3DWCs) have emerged as promising candidates in fan blades due to their high specific strength and stiffness, enhanced delamination resistance, and inherent damage tolerance [2]. Despite their advantages in lightweight applications, fan blades operate under complex loading conditions during service. High-speed rotating fan blades are subjected to centrifugal loads together with vibration loads induced by aerodynamic excitation and mechanical

* Corresponding author.
E-mail address: qiushuang@nuaa.edu.cn (S. Qiu).

vibration. The low-frequency, high-stress centrifugal loading results in low cycle fatigue (LCF), whereas high-frequency, low-stress vibration loading induces high cycle fatigue (HCF), with their interaction leading to combined high and low cycle fatigue (CCF) [3]. Once fatigue failure occurs in fan blades, it can threaten engine safety and structural reliability. Therefore, it is of great engineering significance to investigate the fatigue performance and life prediction of 3DWCs under CCF loading.

Experimental studies form the foundation for understanding material fatigue performance of materials or structures. At present, there are two main types of experimental investigations, namely uniaxial and biaxial combined fatigue tests. For simplicity, some researchers [4-6] adopt uniaxial loading to simulate combined cycle fatigue. For instance, Khoshbakht et al. [4] developed a uniaxial off-axis testing fixture to enable CCF loading. Zheng et al. [5] employed a hybrid stress and strain control method to achieve uniaxial combined cycle fatigue test and then analyzed the interaction effects between HCF and LCF loads. Sarkar et al. [6] designed a two-step loading sequence to investigate on CCF fatigue behavior of 316LN stainless steel at different elevated temperatures. Despite its usefulness in establishing life prediction models, the uniaxial loading approach may not adequately represent the interaction effects associated with multidirectional stress states. To address this limitation, some scholars [7-11] developed test systems capable of applying biaxial fatigue loading. For instance, Oakley et al. [7] achieved biaxial loading tests on blade-like Ti6Al4V specimens by superimposing axial loading and bending excitation. Weser et al. [8] developed a biaxial tension/bending testing system at elevated temperature, employing an electromagnetic shaker and a laser doppler vibrometer to realize excitation and measurement. Despite these advances, existing biaxial testing systems still suffer from load coupling interference, low energy transfer efficiency, and insufficient synchronization accuracy. To this end, Wen et al. [9] designed a non-interfering fixture incorporating nylon tape to achieve the decoupling between HCF and LCF loads. Liu et al. [10] designed a three-hinge fixture to improve the load transfer efficiency and enable the biaxial fatigue loading. Han et al. [11] constructed a testing platform that combines servo loading, electromagnetic excitation, and induction heating to improve the synchronous control accuracy. Although existing biaxial test systems improve the simulation of rotor loading, two main limitations remain, including incomplete load decoupling and insufficient fixture strength for high-strength materials such as 3DWCs. Therefore, a novel biaxial testing system with effective load decoupling and sufficient

structural strength is required for CCF fatigue behavior in 3DWCs.

Research on life prediction models for CCF condition has received extensive attention. At present, there are two main theories: macroscopic phenomenological models and mechanism-based models. In the former category, fatigue life is typically predicted using empirical relationships derived from macroscopic fatigue parameters. For instance, Dimaggio et al. [12] assumed that fatigue loads were independent and used Palmgren-Miner rule to express the fatigue damage as a linear superposition of high cycle and low cycle damage. However, this linear model tends to provide conservative life predictions, as it neglects the coupled effects between different loads. Hence, Zhu et al. [13] proposed a nonlinear interaction damage model based on fatigue characteristic laws. Similarly, Wang et al. [14] introduced HCF stress and maximum stress to account for interaction damage. Liu et al. [15] developed a nonlinear damage model by introducing a modification to the HCF damage term. What more, a nonlinear model was proposed by Yue et al. [16] through the introduction of a damage threshold and the modification of HCF damage. Then, Qiu et al. [17] further improved this approach by proposing a dual-threshold method for the first time. To date, even though the above methods can satisfy design requirements, they are overly dependent on the quantity and validity of test data. Moreover, these methods neglect the evolution of fatigue damage under combined loading conditions. To this end, some scholars [18-21] employed mechanism-based models to investigate the CCF fatigue behavior of metal materials or their structures. Ding et al. [18] developed a two-parameter fatigue model to predict small crack growth. Schweizer et al. [19] proposed a mechanism-based model describing microcracks evolution. Norman et al. [20] identified a threshold value above which fatigue life decreases but remains unaffected below it. This threshold was later quantified as the HCF strain range corresponding to a half reduction in fatigue life [21]. Moreover, several studies [22-24] proposed probabilistic methods to investigate fatigue performance under CCF loading. To sum up, these macroscopic phenomenological models are mainly based on Palmgren-Miner linear cumulative damage rule and its nonlinear expansion. These models are computationally simple and widely used in engineering practice. However, their prediction accuracy and applicability remain limited due to insufficient characterization of damage evolution. In contrast, physics-based models mainly focus on macroscopic crack propagation. Although they capture the interaction effects, their applicability is largely limited to the crack propagation and involves complex computations. Moreover, most existing fatigue models target metallic

materials and structural components, while studies on 3DWCs remain limited. Therefore, it is essential to further develop a reliable model that can predict fatigue life of 3DWCs under biaxial CCF loading.

Existing cumulative fatigue damage models typically employ a single evolution law or deterministic piecewise formulation. Such models may not adequately capture the nonlinear, regime-dependent interaction between the HCF and LCF components under biaxial CCF loading, particularly the gradual transition near the fatigue limit. A multi-region nonlinear framework is therefore needed to represent these distinct interaction regimes and their continuous transition. Accordingly, this study develops a multi-region nonlinear cumulative damage model for fatigue life prediction under biaxial CCF loading. This model introduces the concepts of the weakened damage region, fuzzy damage region, and enhanced damage zone, and quantitatively characterizes them. To account for the uncertainty of HCF contribution, fuzzy logic is employed to model the fuzzy damage region, and the effects of different membership functions on fatigue life prediction are evaluated. Moreover, the dual thresholds, including the HCF and LCF stress amplitude ratio threshold and the fatigue damage threshold, are proposed to reveal the influence of HCF loads and the interaction effects, respectively. This study contributes to the existing literature from three aspects: Firstly, a biaxial experimental platform is established to achieve fatigue behavior of 3DWCs under biaxial CCF loading. This experimental methodology and results provide invaluable insights for engineering applications, especially in aeroengines. Secondly, the model comprehensively incorporates the effect of superimposed HCF loading, based on which the full fatigue characteristic region is divided into three regions. Fuzzy logic is introduced to characterize the damage transition region near the fatigue limit. In other words, the uncertainty of fatigue damage behavior near the fatigue limit is quantified. To the best of our knowledge, few studies have adopted this idea to investigate biaxial fatigue performance. This work provides a new approach for life prediction under biaxial CCF loading. Thirdly, the proposed model can provide more accurate and reliable predictions than other existing models.

The rest of the paper is organized as follows: Section 2 presents the structure of the 3DWCs and the biaxial fatigue testing platform for investigating fatigue behavior under combined tension and bending loading; Section 3 analyses the characteristic parameters involved in the load spectrum, and summarizes the existing linear and nonlinear damage accumulation models; Section 4 poroposes a multi-region nonlinear damage model

under CCF loading; Section 5 validates the model and compares it with other models. Section 6 discusses the effect of the HCF parameters and the potential damage evolution, and Section 7 concludes the research.

2. Experimental methods

2.1. Materials and specimen

3DWCs are textile architectures in which yarn bundles interlace through multiple fabric layers, which enabling integral through-thickness reinforcement and improved structural integrity. The angle-interlock configuration introduces yarn crimp, which enhances tensile performance by improving load transfer capability. In contrast, the straight yarns in the orthogonal configuration provide greater bending stiffness. Furthermore, filling yarns are introduced along the warp direction and alternately interwoven with warp yarns in the weft direction, which further enhances the tensile strength of the structure. This structure combines the tensile advantages associated with crimped yarn paths and the structural stiffness provided by straight yarn segments, thereby exhibiting promising potential for advanced engineering applications.

The internal microstructural characteristics of the material were characterized using X-ray computed tomography (XCT). **Fig. 1** shows the transformation process from the 3D woven architecture to CT cross-sectional slices. **Fig. 1a** presents the schematic configuration of the three-ply twill woven structure, in which three representative cross-sections are defined: the A-A section (**Fig. 1c**), oriented perpendicular to the warp yarns and parallel to the binder yarns; the B-B section (**Fig. 1e**), perpendicular to the binder yarns and parallel to the warp yarns; and the C-C section (**Fig. 1g**), aligned along the weft direction and perpendicular to the binder yarns.

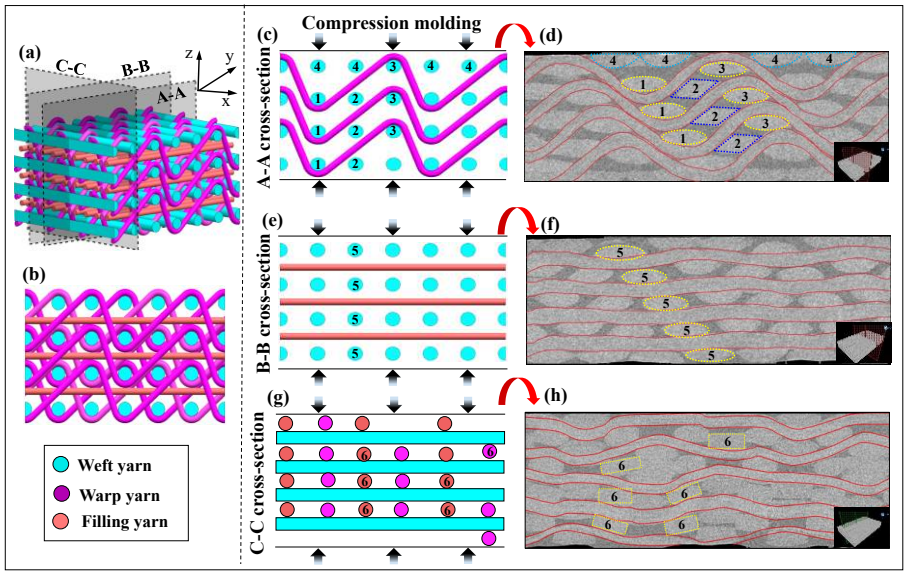


Fig. 1. Schematic of the 3DWCs preform and CT images: (a) 3D view, (b) X-Z plane, (c)A-A cross-section, (d) CT image for A-A cross-section, (e) B-B cross-section, (f) CT image for B-

B cross-section, (g) C-C cross-section and (h) CT image for C-C cross-section.

Following the molding process, 3D woven architecture exhibits several significant microstructural evolutions. **Fig. 1d** illustrates the longitudinal morphology of the warp yarns together with the corresponding weft yarn cross-sections. The warp yarn paths exhibit a periodic wavy configuration, accompanied by localized interlayer contact caused by compaction. Owing to these geometric irregularities, the weft yarn cross-sections present three representative morphologies. At the warp yarn bending regions (positions 1 and 3 in **Fig. 1d**), the cross-sections exhibit a double-convex lens-shaped geometry. Along the inclined segments of the warp yarns (position 2), the cross-sections become approximately parallelogram-shaped. In the highly compressed surface regions (position 4), the yarn cross-sections evolve into single-convex lens-like morphologies. Moreover, mutual extrusion between adjacent yarns during molding induces thickness-directional deflection and local misalignment.

Fig. 1f presents the longitudinal morphology of the filling yarns and their corresponding cross-sectional features. Although the molding process introduces slight deformation to the filling yarns, their overall trajectories remain relatively straight, and the yarn width is largely preserved. Therefore, the filling yarn cross-sections in this region are assumed to maintain a double-convex lens-shaped morphology, as represented by position 5.

Fig. 1h shows the longitudinal morphology and cross-sectional characteristics of the warp yarns. Due to molding-induced compaction, the surface warp yarns are compressed inward, producing an “inward buckling” phenomenon that progressively propagates into the interior yarn layers. The internal yarns become densely packed, leading to severe local compaction within certain regions. In addition, the warp yarn cross-sections undergo compression-induced deformation and predominantly exhibit near-rectangular morphologies, as shown at position 6.

The 3DWCs preform is composed of T800-12K carbon fiber and QY8911-IV bismaleimide resin. The relative mechanical properties of the constituent materials are listed in **Table 1**. The T800-12K carbon fiber and QY8911-IV bismaleimide resin were used as the reinforcement and matrix materials, respectively. The 3DWCs are fabricated through a multi-step process involving 3D preform weaving followed by molding via Vacuum Assisted Resin Transfer Molding (VARTM) process [3].

Table 1

Mechanical properties of component materials.

T800-12K carbon fiber				QY8911-IV bismaleimide resin	
Parameter	Value	Parameter	Value	Parameter	Value
E_{11} (GPa)	294	v_{12}	0.3	E_m (GPa)	4.16
E_{22} (GPa)	19.4	v_{23}	0.4	ν_m	0.34
G_{12} (GPa)	15.0	$X_{11,T}$ (MPa)	5490	$X_{m,T}$ (MPa)	68.44
G_{23} (GPa)	6.9	$X_{11,C}$ (MPa)	2689	$X_{m,C}$ (MPa)	203.28

Note: E_{11} and E_{22} are the longitudinal elastic modulus and transverse elastic moduli; G_{12} and G_{23} are the shear moduli; v_{12} and v_{23} are the Poisson's ratio in different directions, respectively. $X_{11,T}$ and $X_{11,C}$ are the strengths. 'T' and 'C' denote tension and compression, respectively. E_m, v_m, $X_{m,T}$, and $X_{m,C}$ are the elastic moduli, Poisson's ratio, and strength of QY8911-IV bismaleimide resin, respectively.

After molding, the 3DWCs are machined into test specimens to satisfy the experimental dimensions. The specimen geometry is illustrated in **Fig. 2**. It should be noted that the specimen is designed based on the standard provided in ASTM D3039. The standard specimen is designed with dimensions of 230 mm in length, 25 mm in width, and 3 mm in thickness. The open-hole specimen has the same dimensions, with a central hole of 5 mm in diameter. Open-hole specimens under CTBF loading represent practical composite joints, where holes create stress concentrations and secondary bending produces non-uniform stress states. Studying this configuration therefore provides a more realistic assessment of fatigue behaviour and damage initiation in service. Moreover, to reduce stress concentration in the gripping region, unidirectional composite tabs with dimensions of 50 mm in length, 25 mm in width and 3 mm in thickness are bonded to both ends of the specimen. The unidirectional composite shares the same constituent materials as the specimen, ensuring reliable bonding, while its high strength along the fiber direction improves the load-bearing capacity of the gripping region and promotes load transfer during testing.

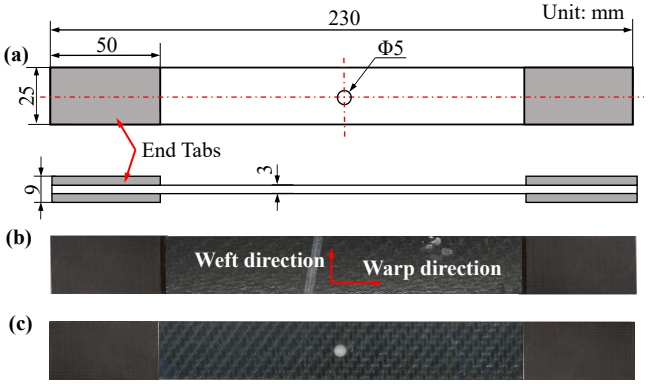


Fig. 2. The specimen for 3DWCs: (a) geometric dimensions, (b) standard specimen and (c) open-hole specimen.

2.2. Experimental system

To investigate the fatigue behavior of 3DWCs, a biaxial combined tension and

bending fatigue (CTBF) loading experimental platform was established, as shown in **Fig. 3**. The platform is composed of a longitudinal tensile loading system, a transverse bending vibration system and a dynamic signal monitoring system. The tentile fatigue load is applied by MTS testing machine and controlled by computer, as shown in **Fig. 3a**. The high cycle vibration load is generated by the signal generator (model: SA-SG030), power amplifier (model: SAPA150) and modal exciter (model: SA-JZ100), as shown in **Fig. 3b**. The signal generator outputs a 2Hz~2kHz sinusoidal signal, which drives the exciter to generate mechanical vibration after power amplification. The test device can achieve lateral displacement in the range of 0~2 mm. The dynamic signal monitoring system includes strain gauge and eddy current displacement sensor (model: 5E102; sampling rate: 1000Hz), which are used to measure the strain and vibration displacement of the sample, respectively. During the test, it is assumed that the temperature change is small, and only the local temperature rise occurs in the later stage. Therefore, it is considered that the temperature rise caused by high cycle vibration can be ignored, and the fatigue damage is mainly dominated by mechanical fatigue.

The critical challenge in CTBF loading test is avoiding the coupling between tensile loading and bending vibration. To address this issue, a dedicated decoupling fixture was designed, employing a winding-type load transfer path to align the transfer axis with the lateral vibration centerline of the specimen, thereby allowing transverse vibration under several tons of tensile load, as shown in **Fig. 3d** and **Fig. 3e**. The fixture consists of an inner clamp, outer clamp, lower clamp, and rotating shaft, through which high-frequency excitation from the electromagnetic shaker is transmitted to the specimen via a threaded rod. Prior to testing, the fixture is mounted on the MTS testing machine, and the specimen is secured between the inner and lower clamps using eight M10 high-strength bolts with controlled torque. Longitudinal tensile loading is applied by the hydraulic MTS system and transferred through a U-shaped fixture and pin connection, while transverse vibration is introduced by the electromagnetic exciter. Vibration amplitude is initiated by gradually increasing the power amplifier output, and the response is recorded by a dynamic data acquisition unit (model: DH5922D). As fatigue damage accumulates and specimen stiffness decreases, the amplifier output is adjusted to maintain constant vibration amplitude while keeping the excitation force unchanged. The test continues until critical stiffness degradation or fracture occurs.

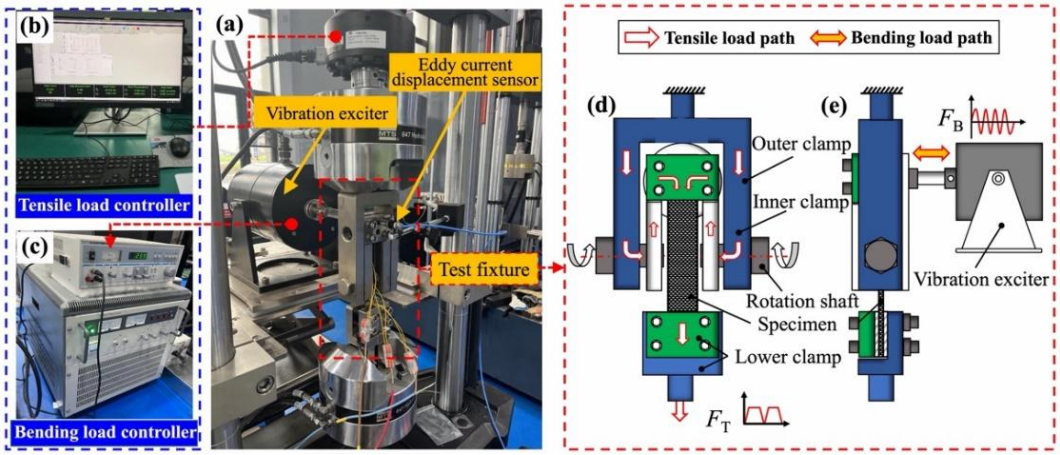


Fig. 3. The CTBF loading platform for 3DWCs. (a) Global set-up, (b) tensile load controller, (c) bending load controller, (d) test fixture for tensile load path and (e) test fixture for bending load path.

Fig. 4 shows the real-time monitoring system for the strain and vibration amplitude under CTBF loading. During testing, the signal generator outputs a sinusoidal signal at a specified frequency, which is amplified and used to drive the exciter to apply transverse vibration to the specimen. A linear eddy-current displacement sensor monitors the vibration response at the excitation point, enabling feedback calibration of the vibration amplitude. Several strain gauges (e.g., 1#, 2#, and 3#) are mounted on the specimen surface to capture local strain responses. All signals are transmitted to a computer via the data acquisition system, where visualization software enables real-time monitoring of strain evolution and crack development.

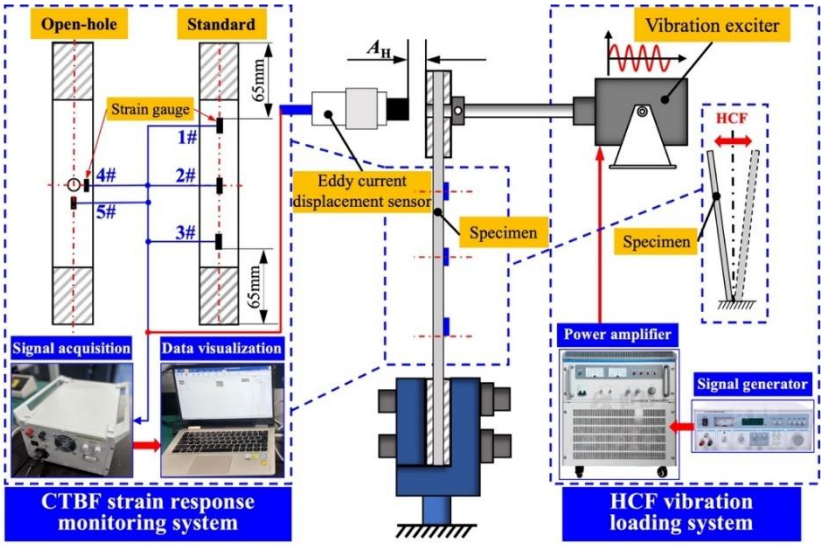


Fig. 4. Real-time monitoring of CTBF strain and HCF amplitude.

2.3. Experimental results

2.3.1. Quasi-static tensile loading

Static tensile tests were conducted on both standard and open-hole specimens to investigate the mechanical properties of 3DWCs. Three specimens were prepared for

each type. The tests were performed on an electronic universal testing machine at a loading rate of 2 mm/min. Surface strain is measured in real time using an MTS extensometer to ensure measurement accuracy.

Fig. 5 shows the stress-strain curves of the standard and open-hole specimens, respectively. Both curves exhibit two distinct stages: a linear stage and a nonlinear stage, which is consistent with previous studies [25][26]. In the linear stage, stress varies linearly with strain, indicating elastic deformation of the material. The slope of this region represents the elastic modulus and corresponds to reversible deformation without damage. In the nonlinear stage, the curve deviates from linearity and gradually bends. This behavior indicates irreversible deformation and damage accumulation within the material, eventually leading to structural failure.

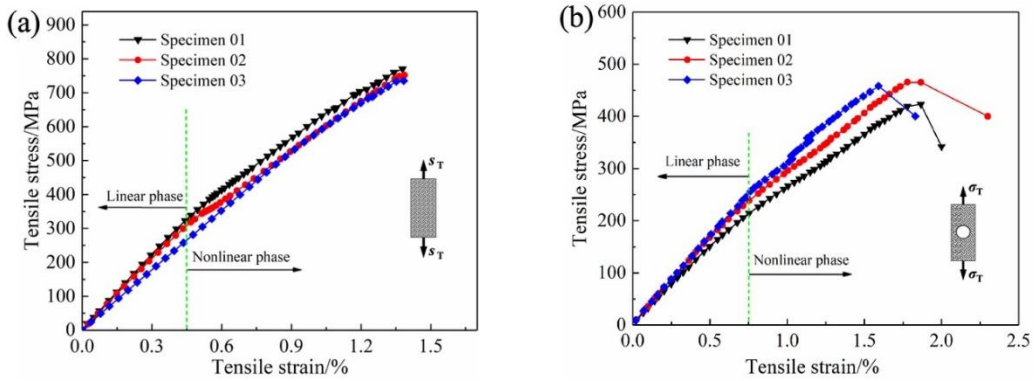


Fig. 5. Quasi-static stress-strain curves: (a) standard and (b) open-hole specimens.

Stiffness and strength are fundamental parameters for characterizing the mechanical performance of materials. The elastic stiffness is obtained by identifying the linear region, while the tensile strength corresponds to the peak stress. The slope of the curve within the strain range of 0.05%-0.25% is used to determine the elastic modulus. As the strain increases, the maximum stress reached on the curve represents the tensile strength of the material.

The tensile stiffness and strength of the specimens are summarized in **Table 2**. The standard specimens exhibit an average tensile stiffness of 68.21GPa and tensile strength of 742.06 MPa. In contrast, the open-hole specimens show an average tensile stiffness of 34.82 GPa and tensile strength of 450.92 MPa, representing reductions of 48.9% and 39.3%, respectively. These results indicate that the presence of a circular hole significantly degrades the tensile performance of the material, with a more pronounced effect on the elastic stiffness.

Table 2

Static tensile test results.

NO.	Tensile	Average	Coefficient	Tensile	Average	Coefficient

	stiffness (GPa)	stiffness (GPa)	of Variation (%)	strength (MPa)	strength (MPa)	of Variation (%)
H01	71.45			763.07		
H02	70.23	68.21	6.73	737.87	742.06	2.60
H03	62.96			725.23		
P01	36.15			463.20		
P02	35.95	34.82	6.14	466.35	450.92	5.33
P03	32.35			423.21		

2.3.2. Dwell tension-tension fatigue loading

Stress-controlled loading with a hold period was adopted for the dwell fatigue tests, during which the maximum tensile stress was maintained for a specified duration. The loading profile was designed to represent the principal variation in centrifugal loading experienced by fan blades under service conditions and to provide a benchmark for the subsequent investigation of combined tension and bending fatigue. **Fig. 6** presents the dwell fatigue loading spectrum. A trapezoidal waveform was employed to represent the characteristic loading sequence associated with take-off (loading), cruise (load holding), and landing (unloading). For experimental feasibility, the duration of the cruise-related hold segment was compressed to 4 s. Therefore, the proposed spectrum represents an accelerated laboratory loading cycle and does not reproduce the actual time scale of a single flight cycle.

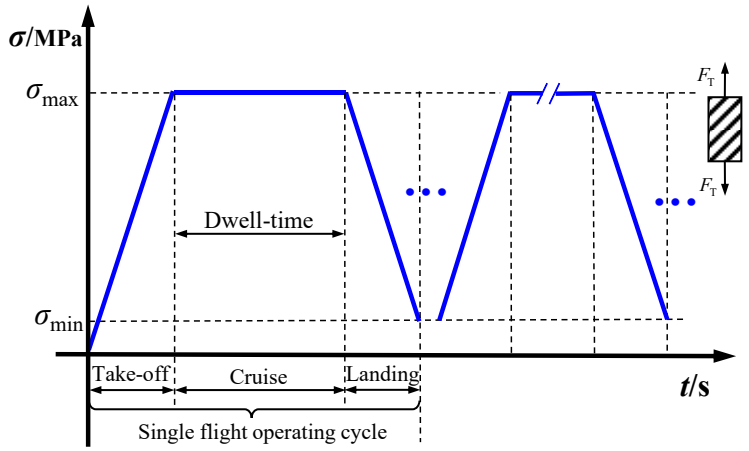


Fig. 6. Load spectrum for dwell tension-tension fatigue test.

During testing, the dwell-time is set to 4s, while both loading and unloading durations are 0.5s. It is noted that the tensile dwell was introduced as a representative laboratory hold segment associated with the cruise stage, rather than as a time-scaled reproduction of the actual cruise duration. This accelerated loading protocol preserves the characteristic loading sequence of the flight cycle while maintaining a practically achievable test duration. In addition, the loading frequency is 0.2Hz. The stress ratio R is maintained at 0.1. The specimen strain is monitored in real time, and response parameters such as the number of cycles (fatigue life) and load-displacement data are

recorded. These results provide essential data for the establishment of fatigue life prediction model. The maximum tensile fatigue stress is normalized as follows:

$$S_T = \frac{\sigma_{max}}{\sigma_{UTS}} \times 100\% \quad (1)$$

where S_T is the normalized maximum stress, hereafter referred to as the stress level, and σ_{UTS} is the ultimate tensile strength of the material.

The stress levels for the dwell fatigue tests are set at 80%, 82%, 85%, and 90% of the tensile strength for standard specimens, and 87%, 90%, and 92% for open-hole specimens. The experimental results are summarized in **Table 3** and **Table 4**, respectively.

Table 3

Dwell tension-tension fatigue results for standard specimens.

NO.	S_T (%)	σ_{max} (MPa)	N_{dwell}	$\bar{N}_{dwell}$
D01	90	668	870	1651
D02		668	1274	
D03		668	2810	
D04	85	630	3005	2643
D05		630	2280	
D06	82	610	4630	6555
D07		610	11162	
D08		610	3872	
D09	80	593	12125	12125

Table 4

Dwell tensile fatigue results for open-hole specimens.

NO.	S_T (%)	σ_{max} (MPa)	N_{dwell}	$\bar{N}_{dwell}$
H01	92	415	2080	3728
H02		415	3080	
H03		415	6024	
H04	90	405	6661	5078
H05		405	4683	
H06		405	3890	
H07	87	392	7455	12038
H08		392	16621	

2.3.3. Biaxial CTBF loading

The actual load spectrum of aircraft structures is typically complex and irregular. It can be transformed into a simplified test spectrum using the damage equivalence principle [28]. Therefore, an equivalent load spectrum used consists of a superposition of trapezoidal and sinusoidal waves, as shown in **Fig. 7**. One load block corresponds to

an outfield flight, including take off, cruise, and landing. The cruise stage is modeled as a constant-stress hold, representing stable loading conditions. In this framework, dwell fatigue corresponds to the stable stress, while bending fatigue represents multiple cyclic stress fluctuations. Each load block therefore includes one stable stress cycle and several equivalent constant-amplitude cycles. The total number of load blocks defines the combined cycle fatigue life.

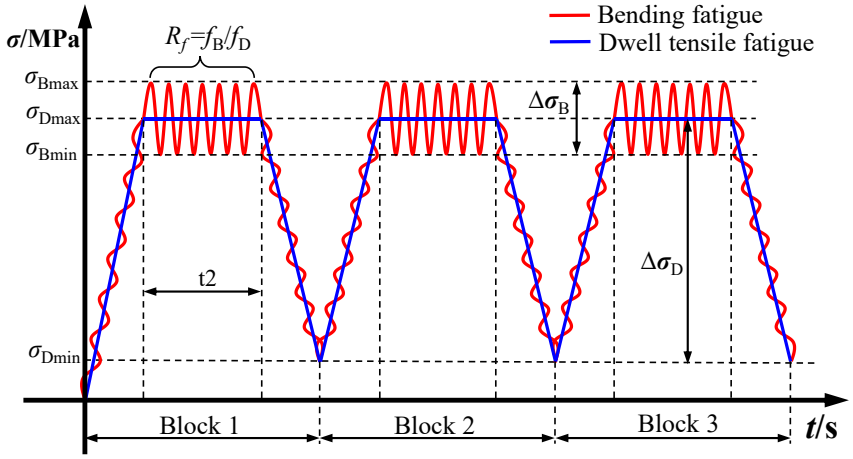


Fig. 7. Load spectrum for the CTBF loading.

The CTBF tests of 3DWCs were conducted under three loading conditions: {S_T=77%, f_B=30Hz}, {S_T=80%, f_B=30Hz} and {S_T=82%, f_B=30Hz}. **Table 5** summarizes the fatigue lives of the standard specimens. In general, the fatigue life decreases with increasing superimposed vibration amplitude, although some overlap occurs among different loading conditions. This scatter is mainly attributed to the stochastic nature of crack initiation and propagation and the sensitivity of fatigue life to the applied stress level. To further illustrate the effects of the loading parameters, the experimental data were fitted as shown in **Fig. 8**. **Fig. 8(a)** presents the S_T-N_{CCF} relationships at different HCF amplitudes, while **Fig. 8(b)** shows the A_H-N_{CCF} relationships at different tensile stress levels. Both sets of fitted curves show that fatigue life decreases as either S_T or A_H increases, indicating the detrimental effects of both tensile stress and superimposed high-frequency vibration on the fatigue resistance of 3DWCs.

Table 5

The results for the standard specimens under CTBF loading.

NO.	S_T (%)	σ_{max} (MPa)	A_H (mm)	N_{CCF}	$\bar{N}_{CCF}$
CS01	77	570	0.3	9610	12301
CS02				14992	
CS03			0.5	13210	9634
CS04				6058	
CS05			0.8	8301	5771
CS06				3241	
CS07	80	593	0.3	13023	8923
CS08				3224	
CS09				10523	
CS10			0.5	7434	6815
CS11				4690	
CS12				8321	
CS13			0.8	2471	3566
CS14				241	
CS15				7985	
CS16	82	610	0.3	2014	5360
CS17				8598	
CS18			0.5	1380	3077
CS19				2229	
CS20				5623	
CS21			0.8	564	1275
CS22				1985	

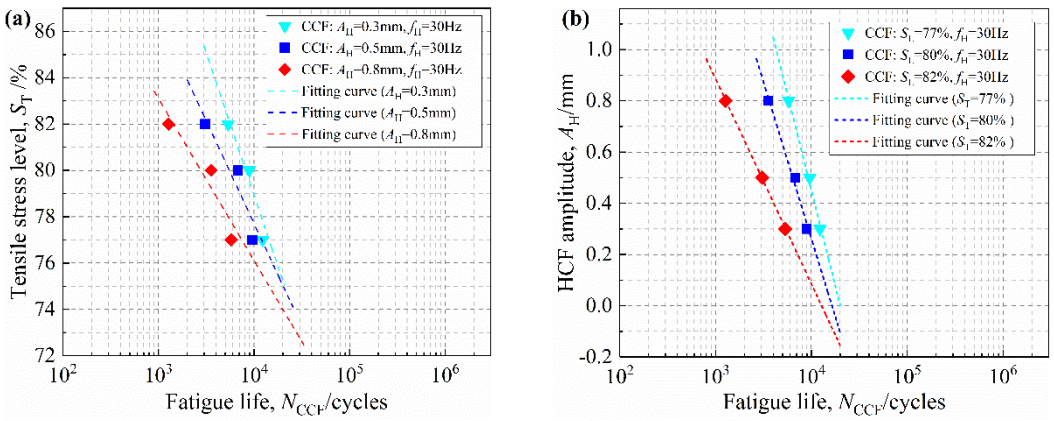


Fig. 8. Fitting results for standard specimens under CTBF loading. (a) The S_T-N_{CCF} curves and (b) A_H-N_{CCF} curves.

Table 6 summarizes the results of the open-hole specimens under different CTBF loading conditions, including{S_T=82%, f_B=30Hz}, {S_T=87%, f_B=30Hz}, and {S_T=90%, f_B=30Hz}. The effect of vibration frequency on fatigue life was further examined at S_T=82% with f_B=30, 50, and 80 Hz. Similar to the standard specimens, some scatter is observed among the fatigue lives under different loading conditions. This scatter may arise from the stochastic nature of crack initiation and propagation, together with the local stress concentration introduced by the open hole. To further characterise the effects of the loading parameters, the experimental data were fitted as shown in **Fig. 9**. **Fig. 9(a)** shows the S_T-N_{CCF} relationships at different HCF amplitudes, while **Fig. 9(b)**

shows the A_H-N_{CCF} relationships at different tensile stress levels. The fitted curves show that fatigue life decreases with increasing S_T or A_H, indicating that higher tensile stress and vibration amplitude accelerate fatigue failure in the open-hole specimens.

Table 6

CTBF loading results for open-hole specimen.

NO.	S_T (%)	σ_{max} (MPa)	A_H (mm)	f_B (Hz)	N_{CCF}	$\bar{N}_{CCF}$
CH01	82	370	0.3	30	32085	28278
CH02					24470	
CH03				50	17406	18848
CH04					20289	
CH05				80	18977	16381
CH06					13785	
CH07					20010	
CH08			0.5	30	15913	14944
CH09					8909	
CH10			0.8	30	2263	5086
CH11					7953	
CH12					5043	
CH13	87	392	0.3	30	7386	7904
CH14					6311	
CH15					10014	
CH16			0.5	30	1219	5714
CH17					6234	
CH18					9690	
CH19			0.8	30	968	1775
CH20					2581	
CH21	90	405	0.3	30	1781	3046
CH22					4311	
CH23			0.5	30	1219	1205
CH24					1706	
CH25					690	
CH26			0.8	30	168	612
CH27					1056	

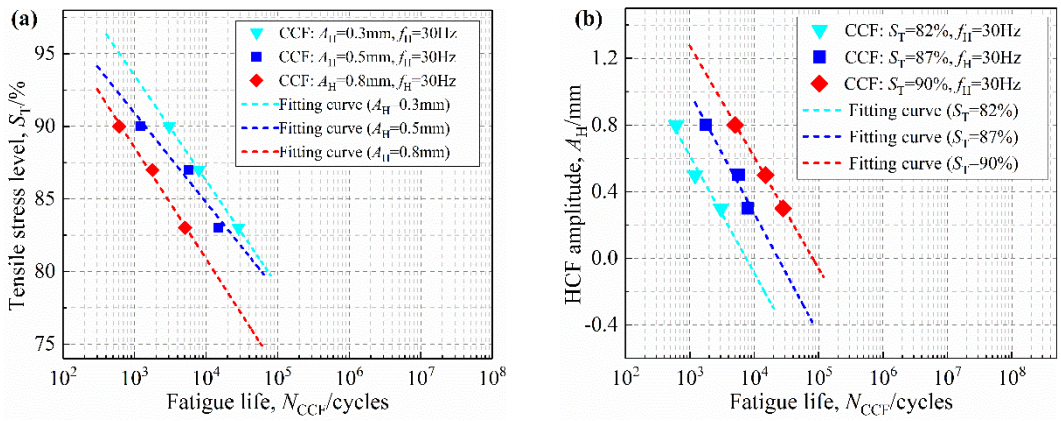


Fig. 9. Fitting results for open-hole specimens under CTBF loading. (a) The S_T-N_{CCF} curves and (b) A_H-N_{CCF} curves.

3. Theoretical analysis for fatigue damage accumulation

3.1. Preliminary parameters definition

The CTBF loading spectrum is characterized by four main parameters: the dwell tensile stress range $\Delta\sigma_{\mathrm{D}}$, the bending stress range $\Delta\sigma_{\mathrm{B}}$, the dwell tensile loading frequency f_{D}, and the bending loading frequency f_{B}, as illustrated in **Fig.7**. These parameters directly influence fatigue life and collectively govern fatigue behavior. Therefore, a comprehensive understanding of their roles is essential for elucidating the variation patterns of fatigue life.

For the dwell fatigue, the stress range $\Delta\sigma_{\mathrm{D}}$ can be calculated as follows:

$$\Delta\sigma_{\mathrm{D}} = \sigma_{\mathrm{Dmax}} - \sigma_{\mathrm{Dmin}} \tag{2}$$

where σ_{Dmax} and σ_{Dmin} represent the maximum stress and minimum stress for the dwell fatigue cycle, respectively.

For the bending fatigue cycle, $\Delta\sigma_{\mathrm{B}}$ can be calculated as follows:

$$\Delta\sigma_{\mathrm{B}} = \sigma_{\mathrm{Bmax}} - \sigma_{\mathrm{Bmin}} \tag{3}$$

where σ_{Bmax} and σ_{Bmin} represent the maximum stress and minimum stress for the bending fatigue cycle, respectively.

There are two parameters, including the frequency ratio R_f and stress amplitude ratio R_σ can be derived from the load spectrum under CCF loading, as follows:

$$R_f = \frac{f_{\mathrm{B}}}{f_{\mathrm{D}}} = \frac{N_{\mathrm{B}}}{N_{\mathrm{D}}} \tag{4}$$

$$R_\sigma = \frac{\Delta\sigma_{\mathrm{B}}}{\Delta\sigma_{\mathrm{D}}} \tag{5}$$

where N_{B} represents the number of the bending fatigue cycles per block and N_{D} is the number of the dwell tensile fatigue cycles. Note that N_{B} can be calculated by $N_{\mathrm{B}} = \mathrm{t}_2 \cdot f_{\mathrm{B}}$ in one block, and f_{B} is the bending fatigue loading frequency. Combined with Eq. (4), R_f can be further expressed by $R_f = N_{\mathrm{B}}$ due to $N_{\mathrm{D}} = 1$ in one block.

3.2. Linear and nonlinear accumulation theories

It is challenging to predict fatigue life due to the need for an accurate description of damage evolution. Although several models have been proposed, a unified and efficient framework is still lacking. In practice, the Palmgren-Miner linear damage model remains the most widely used approach, as follows:

$$D_{\mathrm{sum}} = \sum_{i=1}^{k} \frac{m_i}{N_i} \tag{6}$$

where m_i and N_i are the number of applied cycles and fatigue life corresponding to

the stress level σ_i, respectively. According to the linear theory, the fatigue damage under CTBF loading can be expressed as:

$$D_{\text{sum}} = \sum_{i=1}^{k} k \cdot \left(\frac{1}{N_{\text{T}}} + \frac{m}{N_{\text{B}}} \right) \tag{7}$$

where k is the number of combined loading blocks; m is the number of bending fatigue cycle in one block; N_{T} and N_{B} are the fatigue life for tensile dwell fatigue and bending fatigue, respectively. When the total fatigue damage D_{sum} reaches unity after k blocks for CTBF loading, the material is deemed to have failed due to fatigue. Then, the CTBF life N_{f} can be obtained:

$$N_{\text{f}} = (1+m)\left(\frac{1}{N_{\text{T}}} + \frac{m}{N_{\text{B}}} \right)^{-1} \tag{8}$$

For CTBF loading, the bending frequency is typically much higher than that of dwell tensile fatigue. Consequently, within the same time interval, the number of high-cycle loading events is far greater than that of low-cycle tensile cycles. Although the damage induced by each bending cycle is relatively small, its cumulative effect becomes significant. The frequency ratio R_f and stress amplitude ratio R_σ govern the relative contribution of bending fatigue damage. Therefore, a nonlinear cumulative damage model incorporating an interaction damage term is proposed as follows [13]:

$$D_{\text{sum}} = \sum_{i=1}^{k} k \cdot \left(\frac{1}{N_{\text{T}}} + \frac{m_{\text{B}}}{N_{\text{B}}} + \frac{1}{(\beta+1)\lg(N_{\text{B}})^{\alpha}} \right) \tag{9}$$

where α and β are the stress amplitude ratio and frequency ratio of tensile fatigue loading and bending fatigue loading, respectively.

The above nonlinear cumulative damage model suggests that interaction damage per block is invariant. In fact, the coupling damage between tension and bending loading can follow a decaying trend. In the early fatigue stage, small-amplitude bending vibration loads contribute little to fatigue damage. As damage accumulates toward a critical threshold, the interaction under CTBF loading increases and accelerates damage growth. Hence, interaction damage exhibits stage-dependent nonlinear characteristics throughout the fatigue process rather than remaining constant.

4. Proposed multi-region damage accumulation model

4.1. Identification of the multi-region characteristics

Traditional life prediction models adopt the fatigue limit as the decisive criterion: failure occurs when the applied stress exceeds this limit, whereas stresses below it are assumed to lead to infinite fatigue life. However, in engineering practice, fatigue

damage does not exhibit a sharp boundary. Instead, a fuzzy transition zone exists near the fatigue limit. In other words, the fatigue limit is not an absolute physical constant, but a parameter determined by multiple interacting factors. Its value depends not only on the material's mechanical properties, microstructure, and manufacturing processes, but also on external conditions such as loading conditions and temperature variations. Therefore, fatigue damage initiation near the fatigue limit cannot be clearly defined. More objective criteria are needed to characterize component fatigue behavior.

Compared with dwell fatigue, the biaxial test results generally indicate that the superimposed bending load reduces fatigue life. However, the magnitude of the reduction does not vary proportionally with the bending loading, suggesting a nonlinear interaction between HCF and LCF loading. Although the limited number of tested stress levels does not permit the form of this nonlinear relationship or a distinct transition point to be determined directly, the observed variation motivates two working hypotheses for developing the nonlinear cumulative damage model. First, there is the HCF and LCF stress amplitude ratio (SAR), with a threshold R_{th} that determines whether the bending loading exerts a beneficial or detrimental effect on fatigue life. Second, the fatigue damage (FD), with a threshold D_{th} exists during the fatigue process. The two thresholds describe different physical transitions. The SAR threshold marks the change between loading interaction regimes, whereas the FD threshold identifies the onset of accelerated damage accumulation. Once this threshold is exceeded, the damage growth rate increases. They are introduced as characteristic transition parameters motivated by the observed fatigue response and subsequently calibrated within the model.

Based on the foregoing analysis, a multi-region concept is introduced to describe fatigue behaviour under CTBF loading, as shown in **Fig. 10**. The fatigue domain is divided into three regions according to the stress amplitude ratio: the enhanced damage region (EDR), fuzzy damage region (FDR), and weakened damage region (WDR). The EDR, defined by $R_\sigma \geq R_{\mathrm{th}}$, represents the finite life regime governed by the conventional *S-N* relation. Here, R_{th} is the upper transition threshold marking the departure from the conventional finite-life regime. R_{th} is initially associated with the conventional fatigue-limit level R_0 and serves as the upper boundary of the fuzzy transition region. The FDR, bounded by $R_{\mathrm{F}} < R_\sigma < R_{\mathrm{th}}$, describes the gradual transition near the fatigue limit, where the response exhibits characteristics of both adjacent regions. The lower boundary R_{F} marks the transition to the WDR, in which the damage-enhancing effect of

the superimposed loading becomes comparatively weak. These regions represent different loading-interaction regimes rather than sharply separated damage mechanisms. Based on this framework, a nonlinear cumulative damage model is developed for fatigue-life prediction under CTBF loading.

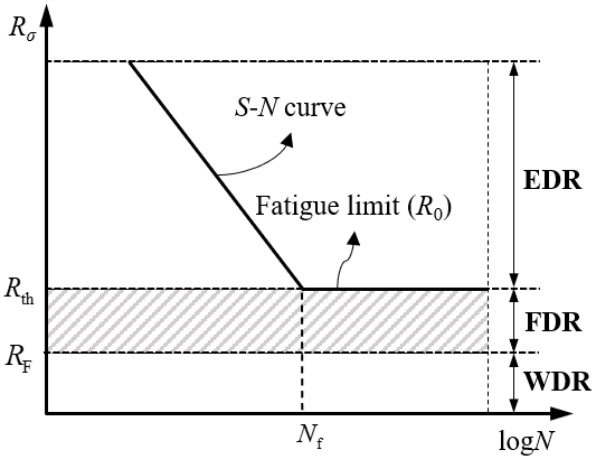


Fig. 10. Multi-region damage mode based on the *S-N* curve.

4.2. Determination of the dual-threshold parameters

Following the previous analysis, the dual-threshold parameters, including the SAR threshold R_{th} and FD threshold D_{th}, sholud be determined in this work. The details will be discussed below.

4.2.1. SAR threshold

The SAR parameter characterizes the relative loading intensity under CTBF loading. Its threshold reflects the influence of bending vibration on the damage accumulation process. This threshold is defined as the SAR value corresponding to the fatigue limit life. Thus, the threshold can be expressed as follows:

$$R_{th} = R_\sigma \left(N_f(\Delta\sigma_D, \Delta\sigma_B) \right) \tag{10}$$

where $N_f(\Delta\sigma_D, \Delta\sigma_B)$ is the fatigue limit life under the CTBF loading; $\Delta\sigma_D$ and $\Delta\sigma_B$ are the DF and BF stress range, respectively.

4.2.2. FD threshold

In this study, the superposition of tension and bending loads induces interaction effect. Fatigue damage threshold is introduced as a critical measure of the resistance to accelerated damage. When the fatigue damage remains below the threshold, the effect of tension and bending loads act independently. Once the threshold is exceeded, the interaction effect intensifies, accelerating crack propagation and shortening fatigue life. Hence, the FD threshold can be quantified as follows:

$$D_{th} = c \cdot D_{eff} \left(1 - \frac{R_\sigma}{R_{th}} \right)^\beta \tag{11}$$

where D_{eff} represents effective tension fatigue damage accumulated over n_{D} cycles and is given by $D_{\text{eff}} = n_{\text{D}}/N_{\text{D}}$; c and β are the material-dependent constants.

For CTBF loading, the initial damage induced by tensile loads governs the fatigue evolution process. In Eq. (11), the effective damage D_{eff} is linearly correlated with the threshold D_{th} and serves as the major factor. In contrast, this term R_σ / R_{th} introduces a secondary modification through the nonlinear term $(1 - R_\sigma / R_{\text{th}})^\beta$. For bending fatigue loading, the stress amplitude varies within a narrow range, exerting limited influence on damage accumulation. Since the R_σ also fluctuates slightly and has a minor effect on damage threshold, β is set to 0.9~0.98. Furthermore, damage threshold is strongly dependent on tensile loading and varies under different loading conditions, the parameter c cannot be reliably determined from fatigue tests alone. Given this, a simplified method is introduced by defining an approximate damage threshold. The bending fatigue damage corresponding to the fatigue limit is taken as an estimate of the damage threshold:

$$D_{\text{th}}^{'} = \frac{n_{\text{B}}}{N_{\text{f}}(\sigma_0)} \tag{12}$$

where n_{B} is the number of bending load cycles contained in one load block, $N_{\text{f}}(\sigma_0)$ is the fatigue life at the fatigue-limit stress amplitud σ_0.

This quantity represents the maximum allowable bending-cycle fatigue damage within single load block. Thus, the parameter c can be obtained through inverse derivation as follows:

$$c = \frac{n_{\text{B}}}{N_{\text{f}}(\sigma_0) D_{\text{eff}}} \left(1 - \frac{R_\sigma}{R_{\text{th}}}\right)^{-\beta} \tag{13}$$

4.3. Fuzzy set theory

4.3.1. Fundamentals of fuzzy logic

Fuzzy set theory, introduced by L.A. Zadeh, provided the first systematic mathematical framework for representing fuzziness. Its central concept is graded membership, which allows sets to describe phenomena with indistinct boundaries. In the present context, fuzzy logic captures the gradual overlap between adjacent damage regimes and avoids the abrupt transitions inherent in deterministic piecewise models. Unlike probabilistic methods, which primarily quantify statistical variability, it is better suited to ambiguous classifications and diffuse regime boundaries. A fatigue state can therefore belong to adjacent regimes to different degrees, providing a more realistic representation of continuous transitions. Membership functions form the basis of this framework by quantifying these degrees of association and enabling the analysis of

fuzzy phenomena.

In classical set theory, let X denote the universe of discourse and $A \in X$ be a subset. For any element $x \in X$, it holds that either $x \in A$ or $x \notin A$, with no intermediate case. Accordingly, a mapping from X to $\{0,1\}$ can be defined as

$$\mu_A : X \to \{0,\ 1\}, \quad x \mapsto \mu_A = \begin{cases} 1, & x \in A \\ 0, & x \notin A \end{cases} \tag{14}$$

Here, μ_A is the characteristic function of the subset A, which is uniquely determined. For $\forall x \in X$, $\mu_A = 1$ if $x \in A$, and $\mu_A = 0$ otherwise. Therefore, the relationship between x and A is characterized solely by the binary distinction of membership or non-membership.

In fuzzy mathematics, the characteristic function μ_A is generalized from the discrete set $\{0,1\}$ to the closed interval [0,1], thereby capturing fuzziness within this interval. On the universe of discourse X, a mapping from X to [0,1] is defined as

$$\mu_{\tilde{A}} : X \to [0,\ 1],\ x \mapsto \mu_{\tilde{A}}(x) \in [0,\ 1] \tag{15}$$

Here, $\tilde{A}$ denotes a fuzzy set on X, and $\mu_{\tilde{A}}(x)$ is its membership function, representing the degree to which the element x belongs to $\tilde{A}$.

The essence of a fuzzy set lies in characterizing the relationship between an element and a set through a membership function. The membership function takes values in the interval [0,1]: when $\mu_{\tilde{A}}(x) = 1$, the element x fully belongs to the fuzzy set A; when $\mu_{\tilde{A}}(x) = 0$, it does not belong to the set at all; and when $0 < \mu_{\tilde{A}}(x) < 1$, x partially belongs to A. The introduction of membership degree thus reflects the characteristic of gradual transition inherent in fuzziness. This core concept constitutes the theoretical foundation for the wide application of fuzzy mathematics in engineering design and complex systems analysis.

4.3.2. Membership function

Fuzzy set theory maps the membership degree of elements to fuzzy concepts to interval [0,1] through membership function. At present, membership function describes the relationship between the index value and the degree of advantages and disadvantages. It can be divided into three categories, including small, medium and large type. The three types constitute the basic function form of fuzzy evaluation. In engineering practice, it is known that membership function can be reasonably selected according to the characteristics of the research object. For the loading conditions below the fatigue limit, the damage behavior presents the fuzzy characteristics of low amplitude stress-induced damage. This work constructs a partial large membership function. Thus, four types of membership function are chosen, as shown in **Fig. 11**, to

perform fuzzy modeling of the stress interval below the fatigue limit.

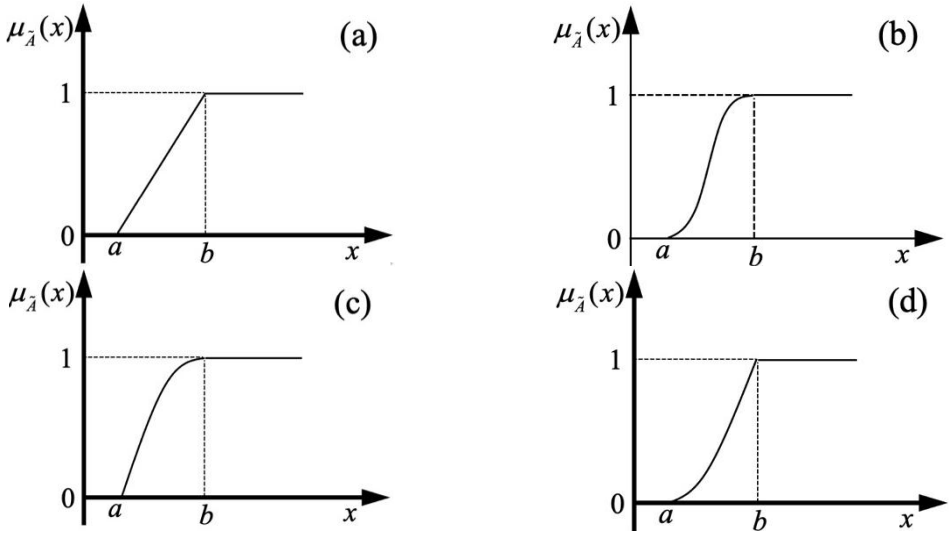


Fig. 11. Large-type membership function. (a) trapezoidal distribution, (b) normal distributio, (c) Γ-type distributio and (d) quadratic parabolic distribution.

4.4. Multi-region damage accumulation model

The damage evolution under CTBF loading exhibits a pronounced nonlinear fatigue performance. It is known that the superimposed bending load may induce microcrack initiation and propagation. This process continuously influences tensile damage, leading to region-dependent damage accumulation mechanisms. According to the previous analysis, a multi-region damage accumulation model incorporating dual-threshold parameters and fuzzy theory is established, as illustrated in **Fig. 12**. There is a notable feature in this model, which is the separate consideration of dominant damage mechanisms under different loading conditions.

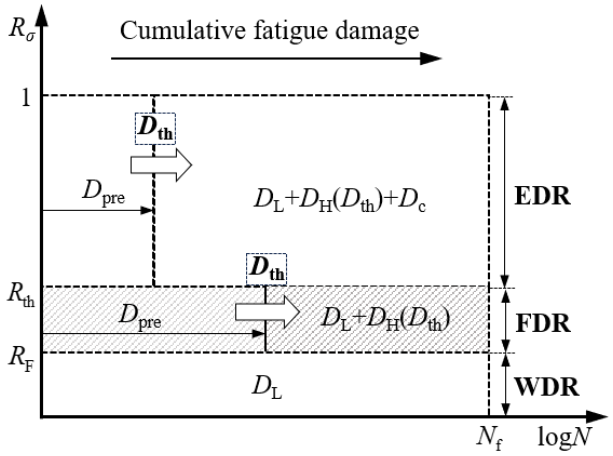


Fig. 12. Multi-region fatigue accumulation damage model.

In the weakened damage region, the stress amplitude of bending loading is small, resulting in limited impact on the fatigue damage. It is primarily governed by tensile fatigue and exhibits only a weakening effect. Hence, a linear damage accumulation model is introduced to account for fatigue damage during the process, as follows:

$$D_{\text{sum}} = D_{\text{T}} = \sum_{i=1}^{k} k \cdot \frac{1}{N_{\text{T}}} \tag{16}$$

where D_{T} is the fatigue damage for tensile dwell fatigue; k is the number of combined fatigue cycles; N_{T} is the fatigue life under the current stress level, which is determined by the *S*-*N* curve.

The increase in the proportion of bending load will lead to a more pronounced evolution of cumulative damage. When the SAR parameter reaches the threshold, the bending load not only significantly influences damage accumulation, but also interacts synergistically with tensile fatigue to accelerate the damage evolution process. Therefore, the critical threshold of the tensile-bending stress amplitude ratio serves as a key indicator for evaluating the contribution of bending load to damage accumulation. From the perspective of cumulative damage mechanics, bending load exhibits distinct threshold effect on damage evolution. If the accumulated damage does not reach this critical threshold, the fatigue-induced damage can be regarded as pre-damage, which is expressed as:

$$D_{\text{pre}} = \sum_{n=1}^{k} k \cdot \left(D_{\text{T}} + D_{\text{B}} \right) \tag{17}$$

where k is the number of combined loading blocks; D_{T} and D_{B} are the tensile fatigue damage and the bending fatigue damage, respectively.

When the initial cumulative damage reaches the critical threshold, bending fatigue accelerates the damage evolution process, and the interaction effect becomes more pronounced. The conventional linear damage accumulation theory is no longer sufficient to capture the nonlinear damage evolution characteristics. Therefore, a modified bending fatigue model incorporating the FD threshold is introduced to characterize its role in the fatigue process. When the accumulated damage reaches this threshold, the total fatigue damage can be expressed as:

$$D_{\text{sum}} = \sum_{n=1}^{k} k \cdot \left(D_{\text{T}} + D_{\text{B}}^{\text{Mod}} \right) \tag{18}$$

$$D_{\text{B}}^{\text{Mod}} = D_{\text{th}} + (1 - D_{\text{th}})^{\beta} D(n)_{\text{B}} \tag{19}$$

where $D_{\text{B}}^{\text{Mod}}$ is an improved bending fatigue damage; $D(n)_{\text{B}}$ is the bending fatigue damage of the n load block; $(1 - D_{\text{th}})^{\beta} D(n)_{\text{H}}$ is the cumulative damage related to bending fatigue after the damage accumulates to the threshold. Here, if $D_{\text{th}} = 0$ the equation degenerates into a pure high cycle fatigue damage model.

In the fuzzy damage region, the SAR value do not approaches the threshold near the fatigue limit. The contribution of the bending fatigue to fatigue damage is uncertain.

Therefore, the fatigue damage induced by single loading block can be described by a fuzzy set $\tilde{D}$. The fatigue damage corresponding to a given SAR value is denoted as $D(R_i)$, whereas the damage associated with the threshold R_{th} is denoted as $D(R_{\text{th}})$. Since fuzzy variables can be characterized by membership functions, the fuzzy damage $\tilde{D}$ below the SAR threshold can be expressed as follows:

$$\mu_{\tilde{D}}(R_i) = \begin{cases} \dfrac{D(R_i)}{D(R_{\text{th}})}, & R_i \in [0, R_{\text{th}}) \\ 1, & R_i \in [R_{\text{th}},\ 1] \end{cases} \tag{20}$$

If the dwell tensile stress remains constant, the total fatigue damage is assumed to be governed primarily by the bending fatigue. Under the two types of stress levels $\sigma_{\text{B},i}$ and $\sigma_{\text{B,th}}$, fatigue damage per loading block can be expressed as:

$$D(\sigma_{\text{B},i}) = m / N_{\text{B},i} \tag{21}$$

$$D(\sigma_{\text{B,th}}) = m / N_{\text{B,th}} \tag{22}$$

where m denotes the number of HCF cycles within a single loading block; $N_{\text{B},i}$ and $N_{\text{B,th}}$ represent the fatigue lives corresponding to the HCF stress levels $\sigma_{\text{B},i}$ and $\sigma_{\text{B,th}}$, respectively.

By substituting Eqs. (21) and (22) into Eq. (20), a fuzzy uncertainty model associated with bending fatigue can be derived, as follows:

$$N_{\text{B},i} = \frac{N_{\text{B,th}}}{\mu_{\tilde{D}}(R_i)}, \quad R_i \in [0, R_{\text{th}}) \tag{23}$$

By combining Eqs. (18), (19), and (23), the fatigue damage model incorporating damage fuzziness can be established, as follows:

$$D_{\text{sum}} = D_{\text{T}} + \left(D_{\text{th}} + (1 - D_{\text{th}})^{\beta} \frac{\mu_{\tilde{D}}(R_i)}{N_{\text{B,th}}} \right) \tag{24}$$

where $N_{\text{B,th}}$ is the fatigue life under the stress level $\sigma_{\text{B,th}}$, and $\sigma_{\text{B,th}}$ corresponds to the bending fatigue stress with the SAR threshold.

In the enhanced damage region, the fatigue damage is governed by both bending fatigue and tension fatigue. The superposition of bending and tensile loading results in a nonlinear damage accumulation, which enhances the initiation and propagation of microcracks.

The interaction effect becomes more complex during the tensile holding stage. In this stage, the fatigue behavior cannot be adequately characterized by the linear damage

accumulation rule; instead, it should be regarded as a threshold-activated nonlinear coupled damage evolution governed by multiple interacting factors. The fatigue damage evolution is influenced not only by the stress level but also by the pre-damage. In this work, we accounts for the effects of bending stress amplitude and tensile pre-damage. Hence, an exponential function law to characterize the coupled damage evolution is adopted, and the expression can be given as follows:

$$D_{\mathrm{Coup}} = \sum_{n_i=1}^{m} (\lambda D_{\mathrm{T}} (\Delta\sigma_{\mathrm{B}})^{\tau} e^{-\eta n_i}) \tag{25}$$

where D_{T} is the low-cycle fatigue damage; $\Delta\sigma_{\mathrm{B}}$ is the bending fatigue stress range; m is the number of bending cycles within a loading block, and i corresponds to the loading block index; λ , τ and η are material constants.

In the enhanced damage region, a similar accelerated damage mechanism exists as that observed in the early stage of the fuzzy damage regime. Once fatigue damage reaches a threshold value, bending fatigue further accelerates accumulation. Thus, by combining Eqs. (18), (19), and (25), the fatigue damage can be derived as follows:

$$D_{\mathrm{sum}} = D_{\mathrm{T}} + D_{\mathrm{B}}^{\mathrm{Mod}} + D_{\mathrm{Coup}} \tag{26}$$

In conclusion, the multi-region damage accumulation model is governed by the characteristics of the three fatigue damage regions. In the weakened damage region, the fatigue damage of the material is primarily governed by tensile fatigue. In the fuzzy damage region, fuzzy mathematics theory is adopted, and membership functions are introduced to characterize the uncertainty of fatigue damage near the SAR threshold. In the enhanced damage region, the interaction effects between tensile and bending loads are described using an exponential function. Therefore, the multi-region accumulation damage model under CTBF loading can be formulated as:

$$D_{\mathrm{sum}} = \begin{cases} D_{\mathrm{T}}, & R_{\sigma} \le R_{\mathrm{F}} \\ D_{\mathrm{T}} + \left(D_{\mathrm{th}} + (1 - D_{\mathrm{th}})^{\beta} \dfrac{\mu_{\tilde{D}}(R_i)}{N_{\mathrm{H,th}}} \right), & R_{\mathrm{F}} < R_{\sigma} < R_{\mathrm{th}} \ \&\ D \ge D_{\mathrm{th}} \\ D_{\mathrm{T}} + D_{\mathrm{B}}^{\mathrm{Mod}} + D_{\mathrm{Coup}}, & R_{\sigma} > R_{\mathrm{th}} \ \&\ D \ge D_{\mathrm{th}} \end{cases} \tag{27}$$

4.5. Fatigue life prediction procedure

Fig. 13 illustrates the fatigue life prediction framework for 3DWCs under CTBF loading. By incorporating dual-threshold parameters and fuzzy theory, the fatigue damage evolution is characterized. In this figure, fatigue damage accumulation model is selected according to the distinct damage characteristics. This ensures the applicability and predictive accuracy of the model across various damage stages.

Firstly, the CCF load spectrum parameters are defined as input variables, including the bending stress amplitude, tension stress amplitude, bending frequency, tension frequency, and the number of bending cycles per block. Meanwhile, the fatigue damage and corresponding fatigue lives are initialized to zero. According to the $S-N$ curve, the pure fatigue lives N_B and N_T are determined, respectively. Then, the relationship of the SAR and fatigue life is employed to identify the SAR threshold.

Secondly, the SAR is compared with its corresponding threshold value to determine the fatigue damage region. (i) When $R_\sigma \le R_F$, fatigue damage is classified within the weakened damage region and can be calculated using Eq. (16). When the fatigue damage reaches the critical value, the cycle is terminated; otherwise, the analysis proceeds to the next loading cycle. (ii) When $R_F \le R_\sigma \le R_{th}$, fatigue damage falls within the fuzzy damage region. Eq. (11) is employed to determine the FD threshold, incorporating the SAR threshold. The fatigue damage per cycle is then calculated using Eq. (17). When $D_{pre} \ge D_{th}$, the cumulative damage from the previous cycles is updated according to Eq. (24). When the fatigue damage exceeds the threshold $D_{sum} \ge 1$, the material fails and the analysis is terminated; otherwise, the next cycle is initiated. (iii) When $R_\sigma \ge R_{th}$, the fatigue damage enters the enhanced damage region. In this region, the modified bending fatigue model (Eq. (19)) and the biaxial fatigue damage model (Eq. (25)) are introduced to characterize the accelerated damage process. The fatigue damage per cycle is calculated using Eq. (26). Once the fatigue damage reaches the critical value, it is terminated; otherwise, the analysis continues to the next cycle.

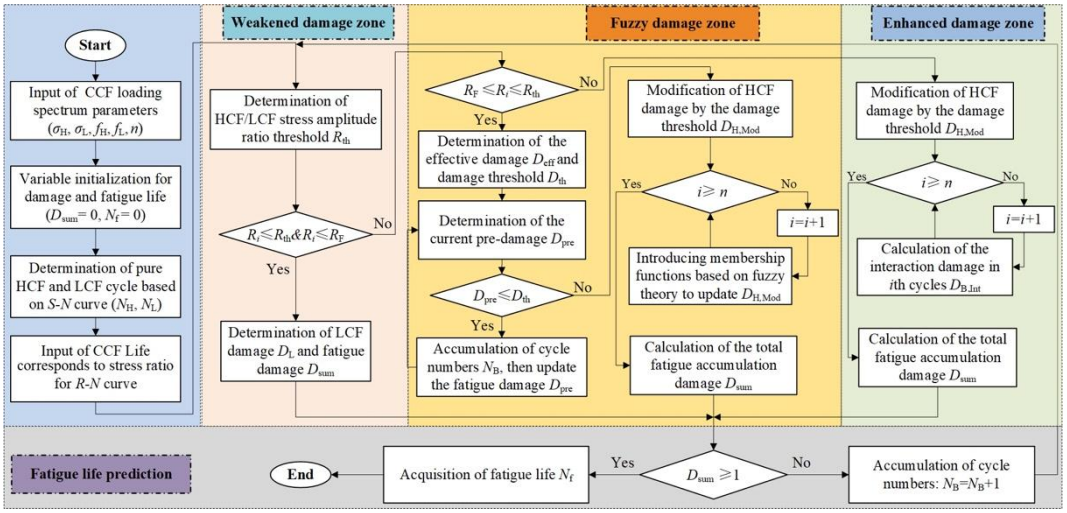


Fig. 13. Flow chart for fatigue life prediction based on multi-region damage.

Finally, when fatigue damage in each region reaches the critical value, the fatigue life N_f is determined, which represents the predicted fatigue life.

5. Model validation and comparison

5.1. Identification of the dual-threshold parameters

In this study, the stress amplitude ratio at fatigue limit is adopted as the threshold parameter for developing the life prediction model. Each loading block is considered equivalent to one tensile fatigue cycle, within which a high-frequency, small-amplitude bending fatigue is superimposed during the load-holding stage. In the study, the number of the 1.0×10^4 loading blocks is defined as the fatigue limit, and the corresponding stress is defined as the stress amplitude ratio threshold parameter.

Fig. 14 illustrates the relationship between the stress amplitude ratio and fatigue life for the standard specimens under CTBF loading. The results indicate that fatigue life decreases markedly with increasing the stress amplitude ratio. When the fatigue life reaches 10^4 cycles, the threshold value of the stress amplitude ratio is 2.31%. Furthermore, a linear correlation is observed between the stress amplitude ratio and the logarithm of fatigue life.

$$\begin{cases} R_\sigma = 18.07 - 1.71\ln(N_{\mathrm{fc}}), & N_{\mathrm{fc}} \le 10^4 \\ R_\sigma = 2.31 & , N_{\mathrm{fc}} > 10^4 \end{cases} \tag{28}$$

Similarly, a negative correlation is observed between the stress amplitude ratio and the fatigue life of the open-hole specimens under CTBF loading, as shown in **Fig. 15**. As the stress amplitude ratio increases, the fatigue life markedly decreases. The stress amplitude ratio threshold corresponding to the fatigue limit is determined to be 2.0%. The fitted relationship can be expressed as:

$$\begin{cases} R_\sigma = 15.39 - 1.46\ln(N_{\mathrm{fc}}), & N_{\mathrm{fc}} \le 10^4 \\ R_\sigma = 2.0 & , N_{\mathrm{fc}} > 10^4 \end{cases} \tag{29}$$

where R_σ is the stress amplitude ratio parameter; N_{fc} is the CTBF life.

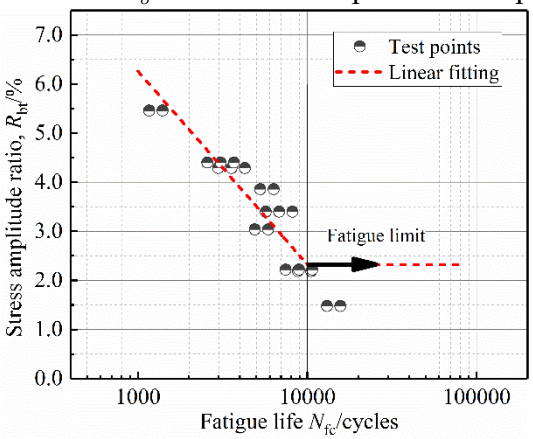


Fig. 14. The relationship between SAR and fatigue life for standard specimens.

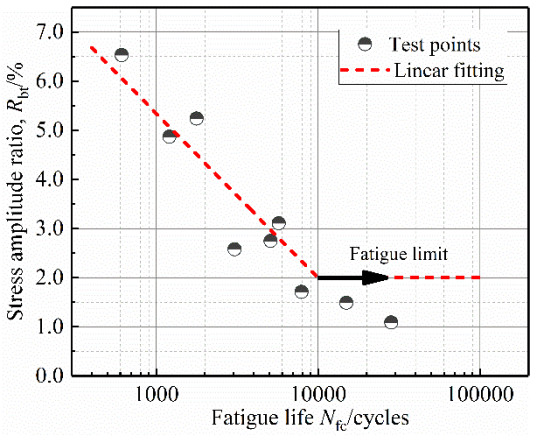


Fig. 15. The relationship between SAR and fatigue life for open-hole specimens.

5.2. Model validation

The multi-region damage accumulation model incorporates membership functions

to reflect the uncertainty of the SAR parameter in the fuzzy damage region. Prior to defining the membership function, it is necessary to determine the upper and lower bounds of the fuzzy damage region. The upper boundary is defined by the SAR corresponding to the fatigue limit. Regarding the lower boundary, when the applied stress is below the fatigue limit, it may still exert a non-negligible influence on fatigue life due to the fuzzy effect [28]. Experimental evidence suggests that this effect typically occurs within 75%~95% of the fatigue limit [29]. Due to their pronounced interlaminar structural complexity and susceptibility to interfacial degradation, composites tend to accumulate damage and initiate microcracks at earlier stages. The onset of the fuzzy effect may occur at comparatively lower stress levels. Therefore, in this study, the lower boundary is conservatively set at 60% of the stress amplitude ratio threshold.

It is known that the modeling of fuzzy regions is not universally applicable to all forms of membership functions. In this study, broader membership functions are selected to more effectively characterize the uncertainty within the stress amplitude ratio interval. Hence, the membership functions can be categorized into three types: (i) linear functions, such as trapezoidal distribution functions; (ii) convex functions, including normal and gamma distribution-based curves; and (iii) concave functions, such as parabolic distribution functions. The distribution characteristics of these functions within the stress amplitude ratio interval [a, b] are illustrated in Fig. 16 and Fig. 17, demonstrating how different functional forms represent varying degrees of uncertainty in the fuzzy region.

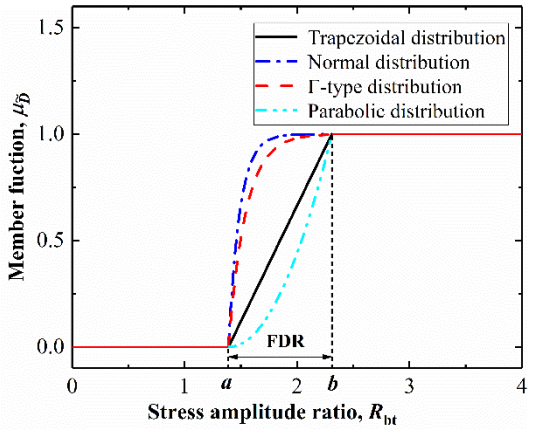


Fig. 16. Different membership functions for standard specimens.

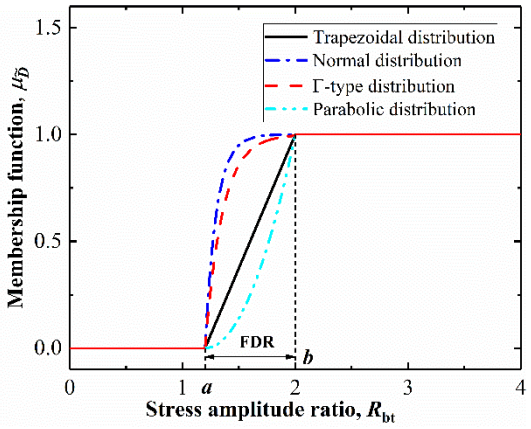


Fig. 17. Different membership functions for open-hole specimens.

To further investigate the influence of different membership functions on fatigue life prediction performance, the aforementioned functions were incorporated into the dual-threshold fatigue life prediction model, followed by a comparative analysis. The

prediction results are summarized in **Table 7**. The table presents the composite fatigue conditions of standard specimens under the stress level of S_T=80%, combined with various bending vibration loads. The results demonstrate that the selection of membership function significantly affects the predicted the fatigue life. The Γ-type distribution achieves the highest prediction accuracy, with the lowest overall relative error. Conversely, the normal distribution produces the largest relative error.

Table 7

Test results for standard specimens under CTBF loading at S_T=80% and f_B=30Hz.

MF	Parameters	R_σ (%)	R_f	N_{exp}	N_{pre}	ε_r (%)
Trapezoidal distribution	a=1.39 b=2.31	2.22	120	8923	7453	16.5
		3.40		6815	5636	17.3
		4.29		3566	3063	14.1
Normal distribution	a=1.39 c=0.20	2.22	120	8923	7031	21.2
		3.40		6815	5214	23.5
		4.29		3566	2871	19.5
Γ-type distribution	a=1.39 k=6.50	2.22	120	8923	8369	6.2
		3.40		6815	6601	3.1
		4.29		3566	3210	9.8
Parabolic distribution	a=1.39 b=2.31	2.22	120	8923	7437	16.8
		3.40		6815	5563	18.4
		4.29		3566	3083	13.6

Table 8 shows the fatigue life prediction results for open-hole specimens at S_T=87%, f_B=30Hz. The results indicate that the choice of membership function significantly influences the accuracy of fatigue life prediction. Among these membership functions, the Γ-type distribution function exhibits the lowest average absolute error of approximately 12%, demonstrating the highest predictive accuracy. In contrast, the normal distribution function yields the largest average error of approximately 21%, resulting in comparatively lower prediction accuracy. Furthermore, the trapezoidal distribution function and quadratic parabolic distribution demonstrate intermediate predictive performance, with error values ranging from approximately 15% to 20%.

Table 8

Test results for open-hole specimens under CTBF loading at S_T=87%, f_B=30Hz.

MF	Parameters	R_σ (%)	R_f	$N_{\exp}$	N_{pre}	ε_r (%)
Trapezoidal distribution	a=1.39 b=2.31	1.71	120	7904	6968	13.4
		3.11		5714	4887	16.8
		5.24		1775	1495	15.9
Normal distribution	a=1.39 c=0.20	1.71	120	7904	9619	-21.6
		3.11		5714	4829	18.3
		5.24		1775	1433	23.8
Γ-type distribution	a=1.39 k=6.50	1.71	120	7904	8831	-11.7
		3.11		5714	5010	12.3
		5.24		1775	1560	12.1
Parabolic distribution	a=1.39 b=2.31	1.71	120	7904	6305	20.2
		3.11		5714	4646	18.7
		5.24		1775	1481	16.5

To sum up, from the distribution characteristics of membership functions, the trapezoidal function is used as a benchmark. The concave-type membership function yields lower membership degrees under identical low-amplitude loading. This leads to smaller cumulative damage and higher fatigue life predictions. In contrast, the convex-type function produces larger membership values under the same loading level. This results in more conservative life predictions. Comparative analysis shows that the Γ-type distribution function achieves the highest prediction accuracy. The normal distribution and quadratic parabolic functions exhibit larger prediction errors. Therefore, the partially large Γ distribution function is adopted in the proposed fatigue life prediction model. This choice improves prediction accuracy and enhances engineering applicability.

5.3. Model comparison

According to the previous analysis, the partially large Γ distribution function is identified as the most suitable membership function for predicting fatigue life. The predictions are conducted for both standard and perforated specimens under various loading conditions. The results are compared with those obtained from the Palmgrem-Miner linear damage model, the improved linear model, and the interaction model to further evaluate the reliability and applicability of the proposed model.

Table 9 presents the predicted results for standard specimens under CTBF loading. It can be seen that the proposed method demonstrates high prediction accuracy across different fatigue loading scenarios. To provide a clearer comparison between the predicted and experimental life values, their distributions within different error bands are illustrated in **Fig. 18**.

Table 9

Comparison of CTBF life predictions for standard specimens.

σ_{L}	A_{H}	R_σ	$N_{\exp}$	N_{pre}

(MPa)	(mm)	(%)		Palmgrem-Miner model	Modified Miner model	Zhu's interaction model [13]	Proposed model
570	0.3	1.48	12301	18369	14658	10087	11268
	0.5	2.19	9634	17250	12023	6930	10568
	0.8	3.86	5771	9890	6875	3890	6520
593	0.3	2.22	8923	10325	9968	6635	8369
	0.5	3.40	6815	9501	7830	4680	6601
	0.8	4.29	3566	7201	4980	2021	3210
630	0.3	3.04	5360	8895	6758	3603	4930
	0.5	4.40	3077	6681	4680	1360	3512
	0.8	5.46	1275	3683	1735	668	1620

As shown in **Fig. 18**, all four life prediction models yield results within the ±3.0 error band, indicating overall acceptable predictive performance. However, notable discrepancies are observed among the models. The Palmgren–Miner rule and its improved variants tend to produce relatively conservative predictions, whereas Zhu's interaction model yields comparatively more aggressive estimates, with most results still falling within the ±3.0 error band. In contrast, the multi-region damage accumulation model incorporating fuzziness demonstrates superior predictive capability. Its predictions are symmetrically distributed about the reference line, with the majority concentrated within the ±1.5 error band, indicating enhanced accuracy and greater adaptability under varying loading conditions.

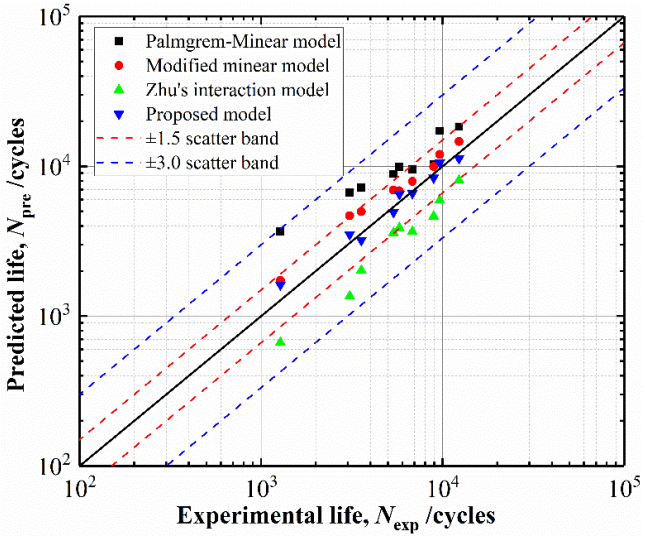


Fig. 18. Comparison between test results and predicted lives for standard specimens.

Table 10 resents the predicted results for open-hole specimens under CTBF loading. The proposed model maintains relatively high prediction accuracy across different fatigue scenarios. To further illustrate the deviation between predicted and experimental lives, **Fig. 19** shows their distribution within different error bands.

Table 10

Comparison of CTBF fatigue life predictions for open-hole specimens.

σ_L (MPa)	A_H (mm)	R_σ (%)	N_{exp}	N_{pre}			
				Palmgrem-Miner model	Modified miner model	Zhu's interaction model	Proposed model
370	0.3	1.09	28278	46253	40231	15123	37201
	0.5	1.49	14944	32124	28653	8259	19230
	0.8	2.75	5086	7598	6632	4230	5600
393	0.3	1.71	7904	9610	10112	4871	8831
	0.5	3.11	5714	6574	7536	2687	5010
	0.8	5.24	1775	3623	3120	3251	1560
406	0.3	2.58	3046	4635	5300	1231	3210
	0.5	4.87	1205	3600	3101	823	1608
	0.8	6.53	612	890	1023	489	750

As shown in **Fig. 19**, the predicted points obtained from the proposed model are primarily located within the ±1.5 error band and distributed near the isoline. This indicates strong agreement between predicted and experimental results. The findings demonstrate that the life prediction model incorporating different zoning characteristics can effectively predict fatigue life. For the existing damage accumulation models, the Miner model and its improved variant exhibit similar prediction accuracy but tend to produce conservative estimates. The Zhu's interaction model shows relatively good accuracy in the low-life region. However, its prediction performance decreases significantly in the high-life region. For the existing models, most results fall within the ±3 error band. In contrast, the proposed model maintains high prediction accuracy across the entire life range. This confirms the rationality and adaptability of introducing a fuzzy approach under CTBF loading.

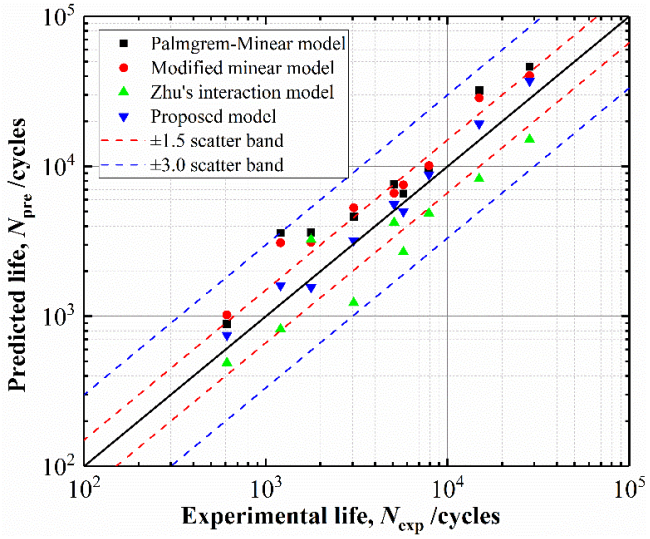


Fig. 19. Comparison between test results and predicted lives for open-hole specimens.

6. Discussion

The findings of this study suggest that the proposed multi-region modelling approach can effectively predict fatigue life of the 3DWCs under biaxial CCF loading. This section further examines the influence of HCF parameters (A_H, f_H) on fatigue performance. The introduction of transverse HCF loading is identified as a primary source of uncertainty in the fracture location. Moreover, the probable damage evolution is discussed based on the underlying microscopic failure mechanisms.

6.1. Effect of the HCF parameters

As can be seen from Section 2.3, the superposition of HCF vibration on LCF loading leads to a reduction in fatigue life. To quantify this effect, an indicator termed life reduction rate is defined as the relative reduction in CCF life with respect to pure LCF life. In other words, the pure LCF life serves as the baseline reference. **Fig.20** shows a consistent reduction in fatigue life for open-hole specimen with increasing vibration amplitude and frequency (A_H, f_H) across tensile stress levels (S_T).

In **Fig. 20a**, for S_T = 82%, the life reduction increases from 26.8% to 60.1% as A_H rises. This result shows a clear influence of HCF on fatigue degradation even at a relatively low LCF stress level. In **Fig. 20b**, for S_T = 87%, the life reduction increases from 34.3% to 85.2%. The magnitude of reduction is higher than that in **Fig. 20a**, which reflects a stronger response of fatigue life to HCF loading at an elevated stress level. In **Fig. 20c**, for S_T = 90%, the life reduction reaches up to 87.9%. The decrease in fatigue life becomes more pronounced at higher amplitudes, indicating a rapid transition to a severe damage state under combined loading. Overall, the results reveal a nonlinear coupling between LCF and HCF. The combined loading produces a stronger damage effect than a linear superposition. This behavior highlights the importance of considering interaction effects in fatigue life prediction under CCF conditions.

In **Fig. 20d**, fatigue life reduction with increasing vibration frequency exhibits a clear but nonlinear decreasing trend. A distinct change occurs at 30 Hz, suggesting a mechanistic transition or critical interaction between loading components. Beyond this point, the rate of life degradation stabilizes. This behavior is also linked to the increasing difficulty of maintaining vibration amplitude at higher frequencies. Notably, despite the reduction, fatigue life remains within the same order of magnitude, reflecting the dominance of LCF characteristics. Therefore, within the studied range, the influence of frequency on fatigue life is relatively limited, while vibration amplitude plays a more significant role.

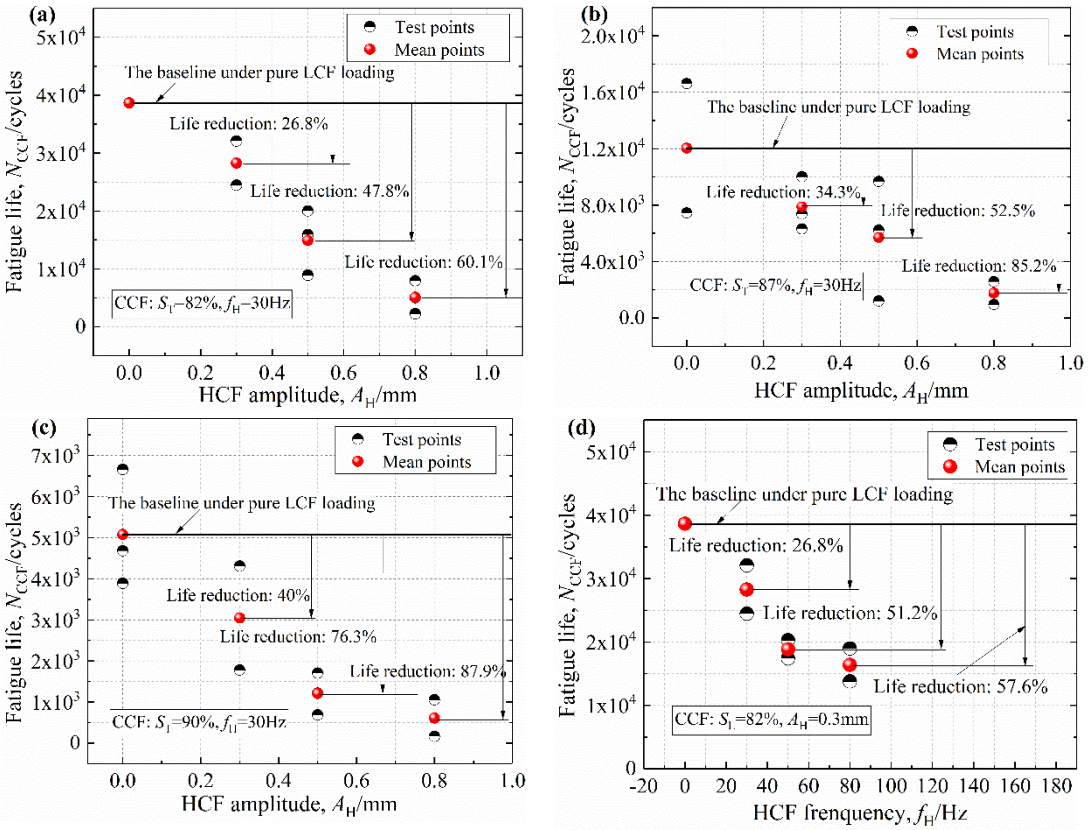


Fig. 20. Baseline-relative fatigue life reduction rate for open-hole specimen: (a) S_T=82%, f_H=30Hz; (b) S_T=87%, f_H=30Hz; (c) S_T=90%, f_H=30Hz; (d) S_T=82%, A_H=0.3mm.

6.2. Potential damage evolution mechanism

The coupled effects of microstructural characteristics and external loading in 3DWCs commonly govern damage initiation and propagation under biaxial CCF loading. Furthermore, internal features, including fiber architecture, matrix cracking, fiber/matrix failure and interfacial debonding, may evolve differently under varying cyclic loading conditions. Consequently, the fatigue failure behavior of 3DWCs is highly complex due to the interaction among multiple microstructural damage mechanisms. To further elucidate the influence of loading conditions, this section discusses the dominant damage and failure mechanisms of 3DWCs under different damage states.

Based on the two threshold parameters (R_{th}, D_{th}) mentioned in Section 4.2, a schematic diagram illustrating the dominant damage mechanisms under different states is presented in **Fig. 21**. As shown in the figure, the damage evolution is strongly related to the interaction among the warp yarns, weft yarns, filling yarns, and the surrounding matrix. The stress concentration initially occurs at the yarn interfaces, leading to local interface debonding and fibre/matrix damage under biaxial CCF loading.

Fig. 21a shows the microscopic damage mechanism in the weakened damage state.

In this case, the current R_σ is less than the critical value R_{th}. Although the HCF loads are small, they may complicate the damage mechanisms due to the weak interfacial and matrix strengths. Thus, only localized damage initiates within the structure, including minor matrix cracking, limited fibre/matrix failure, and small regions of interface debonding near the warp yarns. Since the damage is still isolated and non-propagating, the overall structural integrity and stiffness are only slightly affected.

Fig. 21b shows the microscopic damage mechanism in the fuzzy damage state. In this case, the current R_σ increases but remains below the critical threshold R_{th}. The damage progressively develops and spreads throughout the woven architecture as cyclic loading continues. Interface debonding becomes more ronounced in the yarn waviness regions, while matrix cracks begin to connect and local fibre/matrix failures increase. Once the damage exceeds the critical threshold, noticeable stiffness degradation occurs and multiple damage mechanisms start interacting with each other.

Fig. 21c shows the microscopic damage mechanism in the enhanced damage state. In this case, the current R_σ is larger than the critical value R_{th}. The typical damage accumulates throughout the composite and approaches the failure condition. Large-scale interface debonding, interconnected matrix cracks, and widespread fibre/matrix failures severely weaken the load transfer capability between yarns. Cracks propagate extensively across adjacent yarn layers and through the thickness direction, resulting in significant degradation of the load-bearing capability and eventual structural failure of the composite.

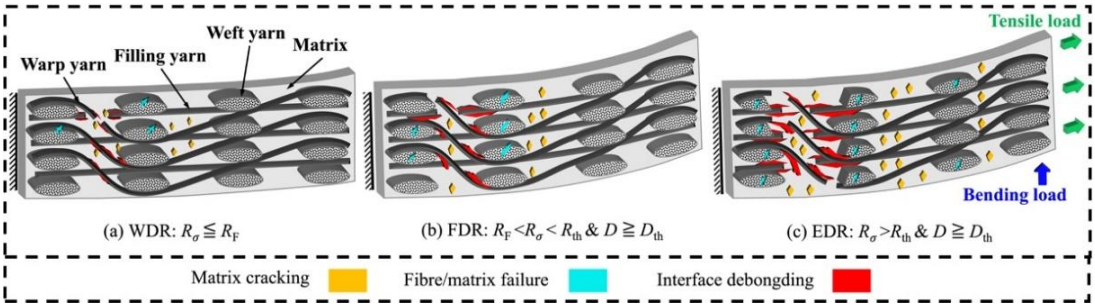


Fig. 21. The damage evolution of 3DWCs under biaxial CCF loading.

7. Conclusions

This work developed a multi-region nonlinear model to predict the fatigue life of 3DWCs under biaxial CCF loading. The model comprehensively considers the loading conditions involving superposed HCF loads and proposes different damage evolution mechanisms for different loading regimes. some test data are applied to validate the accuracy of the model. Several meaningful conclusions can be summarized as:

(1) By introducing the concept of the SAR ratio (R_σ) and its threshold (R_{th}), where

the threshold is determined based on the fatigue limit under combined HCF and LCF loading, a quantitative fatigue damage threshold parameter (D_{th}) was established by integrating the effective damage parameter with the current stress amplitude ratio. When $R_\sigma < R_{th}$, the influence of HCF on the overall damage evolution is limited to minor perturbations. However, when $R_\sigma \geqq R_{th}$, the superposed HCF loads significantly accelerate damage propagation, induce nonlinear cumulative effects, and ultimately lead to a substantial reduction in fatigue life.

(2) The effects of different loading conditions on fatigue damage characteristics were systematically investigated. The fatigue damage evolution can be classified into three regimes: the enhanced damage region(EDR), the fuzzy damage region(FDR), and the weakened damage region(WDR). In the EDR state, the coupled interaction between HCF and LCF dominates the damage evolution, and a load-coupling term is introduced to characterize the acceleration effect induced by HCF loading. In the FDR state, the damage evolution is primarily governed by LCF, accompanied by threshold-activated HCF contributions, while the associated uncertainty is represented using a skewed membership distribution function. In the WDR state, the influence of HCF loading becomes negligible, and the damage evolution mainly follows the linear cumulative behavior dominated by LCF.

(3) Fatigue life prediction studies of 3DWCs under CTBF loading were conducted using both standard and open-hole specimens. These models were established based on different damage regimes. The results indicate that the Γ-type distribution function provides the minimum prediction error. Further comparisons under different loading conditions demonstrate that the traditional Palmgren-Miner linear cumulative damage model and its modified versions tend to yield conservative predictions, whereas the coupled damage model proposed by Zhu exhibits relatively aggressive predictions. The prediction errors of these existing models are mainly distributed within the error band of 1.5 to 3.0. In contrast, the proposed life prediction model maintains prediction errors within ±1.5, demonstrating higher prediction accuracy and stronger adaptability under varying loading conditions.

The proposed model is a phenomenological life prediction framework calibrated for the 3DWCs under CCF loading. Its experimental validation is currently limited to

fatigue life. The damage evolution has not been independently verified. The woven architecture and notch effects are implicitly embedded in the calibrated parameters, and application to other materials, hole geometries, or loading conditions requires separate calibration and validation.

Funding Declaration

We greatly acknowledge the financial support from National Science and Technology Major Project (Grant No. 2017-IV-0007-0044) and National Natural Science Foundation of China (Grant No. 52175142).

References

[1] Wei J, Zhang Y, Liu Y, et al. Advances in resin matrix composite fan blades for aircraft engines: A review[J]. Thin-Walled Structures, 2024, 202(000): 57.

[2] Ali M A, Umer R, Khan K A, et al. non-destructive evaluation of through-thickness permeability in 3D woven fabrics for composite fan blade applications[J]. Aerospace Science and Technology, 2018, 82-83: 520-533.

[3] Qiu S, Cui H, Zhang H. Investigation on fatigue behavior and failure mechanism of quasi-3D woven composites under combined high and low cycle fatigue[J]. International Journal of Fatigue, 2025, 193:108768.

[4] Khoshbakht M, Chowdhury S J, Seif M A, et al. Failure of woven composites under combined tension-bending loading [J]. Composite structures, 2009, 90(3): 279-286.

[5] Zheng X, Engler-Pinto Jr C C, Su X, et al. Modeling of fatigue damage under superimposed high-cycle and low-cycle fatigue loading for a cast aluminum alloy [J]. Materials Science and Engineering: A, 2013, 560: 792-801.

[6] Sarkar A, Nagesha A, Parameswaran P, et al. Evolution of damage under combined low and high cycle fatigue loading in a type 316LN stainless steel at different temperatures[J]. International Journal of Fatigue, 2017, 103: 28-38.

[7] Oakley SY, Nowell D. Prediction of the combined high- and low-cycle fatigue performance of gas turbine blades after foreign object damage[J]. International Journal of Fatigue, 2007, 29(1):69-80.

[8] Weser S, Gampe U, Raddatz M, et al. Advanced experimental and analytical investigations on combined cycle fatigue (CCF) of conventional cast and single-crystal gas turbine blades[J]. Turbo Expo: Power for Land, Sea, and Air, 2011, 54662: 19-28.

[9] Banning W, Shaolin L, Duoqi S, et al. Combined cycle fatigue test technology for composite materials[J]. Journal of Aerospace Power, 2025,40(01):346-352.

[10] Liu L, Gao HS, Wang JD, et al. Combined high and low cycle fatigue analysis of FGH96 alloy under high temperature conditions[J]. Materials Today Communications, 2024, 38:108053.

[11] Han L, Huang D, Yan X, et al. Combined high and low cycle fatigue life prediction model based on damage mechanics and its application in determining the aluminized location of turbine blade[J]. International Journal of Fatigue, 2019, 127: 120-130.

[12] Dimaggio D, Riva A, Bardetta C, et al. Fatigue assessment of a notched member under combined LCF and HCF loading [J]. Procedia Structural Integrity, 2017, 7: 198-205.

[13] Zhu S P, Yue P, Yu Z Y, et al. A combined high and low cycle fatigue model for life prediction of turbine blades [J]. Materials, 2017, 10(7): 698.

[14] Wang X, Hou J, Guo H, et al. A Miner's rule-based fatigue life prediction model for combined high and low cycle fatigue considering loading interaction effect [J]. Fatigue & Fracture of Engineering Materials & Structures, 2023, 46(12): 4525-4540.
[15] Liu P, Wang X, Shen Q, et al. A nonlinear cumulative fatigue damage life prediction model under combined cycle fatigue loading considering load interaction [J]. International Journal of Fatigue, 2023, 177: 107972.
[16] Yue P, Ma J, Huang H, et al. Threshold damage-based fatigue life prediction of turbine blades under combined high and low cycle fatigue [J]. International Journal of Fatigue, 2021, 150:106323.
[17] Qiu S, Cui H, Zhang H, et al. A dual-threshold modelling approach for fatigue life prediction under combined high and low cycle fatigue [J]. International Journal of Fatigue, 2022, 164:107110.
[18] Ding J, Hall R F, Byrne J. Fatigue crack growth from foreign object damage under combined low and high cycle loading. Part II: A two-parameter predictive approach [J]. International journal of fatigue, 2007, 29(7):1350-1358.
[19] Schweizer C, Seifert T, Nieweg B, et al. Mechanisms and modelling of fatigue crack growth under combined low and high cycle fatigue loading [J]. International Journal of Fatigue, 2011, 33(2): 194-202.
[20] Norman V, Skoglund P, Leidermark D, et al. Thermo-mechanical and superimposed high-cycle fatigue interactions in compacted graphite iron [J]. International journal of fatigue, 2015,80: 381-390.
[21] Norman V, Skoglund P, Leidermark D, et al. The effect of superimposed high-cycle fatigue on thermo-mechanical fatigue in cast iron [J]. International Journal of Fatigue, 2016, 88: 121-131.
[22] Gao H F, Zio E, Wang A, et al. Probabilistic-based combined high and low cycle fatigue assessment for turbine blades using a substructure-based kriging surrogate model[J]. Aerospace Science and Technology, 2020, 104: 105957.
[23] Han L, Chen C, Guo T, et al. Probability-based service safety life prediction approach of raw and treated turbine blades regarding combined cycle fatigue [J]. Aerospace Science and Technology, 2021, 110: 106513.
[24] Bai S, Li Y F, Huang H Z, et al. A probabilistic combined high and low cycle fatigue life prediction framework for the turbine shaft with random geometric parameters[J]. International Journal of Fatigue, 2022, 165: 107218.
[25] Song J, Wen W, Cui H. Experimental and numerical investigation of mechanical behaviors of 2.5 D woven composites at ambient and un-ambient temperatures [J]. Composite Structures, 2018, 201: 699-720.
[26] Guo J, Wen W, Zhang H, et al. Representative cell modeling strategy of 2.5D woven composites considering the randomness of weft cross-section for mechanical properties prediction [J]. Engineering Fracture Mechanics, 2020, 237(1): 107255.
[27] Wang R, Wei J, Hu D, et al. Investigation on experimental load spectrum for high and low cycle combined fatigue test [J]. Propulsion and Power Research, 2013, 2(4): 235-242.
[28] Zhu SP, Huang HZ, Wang ZL. Fatigue life estimation considering damaging and strengthening of low amplitude loads under different load sequences using fuzzy sets approach. International Journal of Damage Mechanics, 2011,20(6):876-899.

[29] Xi L, Songlin Z. Strengthening and damaging under low-amplitude loads below the fatigue limit [J]. International Journal of Fatigue, 2009, 31(2): 341-345.

Supplementary Files

This is a list of supplementary files associated with this preprint. Click to download.

- Table.docx